Unique composition and evolutionary histories of large low velocity provinces

This manuscript is a non-peer reviewed preprint submitted to EarthArXiv. The manuscript has been submitted for peer review in Scientific Reports.

James Panton[1*], J. Huw Davies[1], Paula Koelemeijer[2], Robert Myhill[3], Jeroen Ritsema[4]

[1*]School of Earth and Environmental Sciences, Cardiff University, Park Place, Cardiff, CF10 3AT, Wales, UK.
[2]Department of Earth Sciences, University of Oxford, South Parks Road, Oxford, OX1 3AN, England, UK.
[3]School of Earth Sciences, University of Bristol, Queens Road, Bristol, BS8 1RJ, England, UK.
[4]Department of Earth and Environmental Sciences, University of Michigan, 1100 North University Avenue, Ann Arbor, 40819, MI, USA.

*Corresponding author(s). E-mail(s): pantonjc@cardiff.ac.uk;

Abstract

The two "large low velocity provinces" (LLVPs) are broad, low seismic wave speed anomalies in Earth's lower mantle beneath Africa and the Pacific Ocean. Recent research suggests they contain relatively dense subducted oceanic crust (SOC), but the relative concentration of this recycled material within them is an open question. Using simulations of 3-D global mantle circulation over the past 1 Gyr, we find that two antipodal LLVPs develop naturally as a consequence of Earth's recent subduction history and the gravitational settling and stirring of SOC. Shear-wave velocity reductions in the two LLVPs are similar due to the dominating influence of temperature over composition. However, the formation histories are distinct. Circum-Pacific subduction of oceanic lithosphere has continuously replenished the Pacific LLVP with relatively young SOC since 300 Ma, while the African LLVP comprises older, well-mixed material. We estimate that the Pacific LLVP is enriched in SOC by up to 53% compared to the African

LLVP and therefore more dense and less buoyant, potentially contributing to the height difference between the two structures.

1 Introduction

The large low velocity provinces (LLVPs) are broad seismic wave speed anomalies in the lower mantle beneath the Pacific and Africa [1]. Their composition, formation, and longevity have been the focus of many geodynamic and seismological investigations [1–3]. These studies have revealed that LLVPs represent anomalously hot regions [4] with a different bulk chemistry than the ambient mantle and that their locations and geometries are strongly influenced by Earth's subduction history [5–7]. The wave speed reductions are 1% to 3% in both the African and Pacific LLVPs [8] but the African LLVP may reach up to 550 km higher above the core-mantle boundary (CMB) than its Pacific counterpart [9, 10]. In addition, there may be lateral isotopic variations within each LLVP [11] as well as depth variations in bulk composition [12].

There are two end-member views on the formation of thermo-chemical LLVPs. One is that the LLVPs may be enriched in iron-rich, primitive crust [12] or other primordial material [13, 14] that has resisted entrainment into the convecting mantle [15]. Primordial enrichment may be the result of upside down differentiation [16] or the moon-forming impact of the proto-Earth with Theia [17]. Alternatively, and the point of view we take in this study, LLVPs may be areas of lower mantle which are enriched in subducted oceanic crust (SOC) [18, 19] which are replenished continuously by subduction [20, 21].

While there have been numerous studies into the formation of LLVPs from a dense primordial layer [e.g. 22–24], studies of the contribution of SOC to LLVP formation have largely been limited to 2D geometry [20, 25, 26]. From such studies we have learnt that the intrinsic (chemical) density of SOC strongly controls the lateral extent of thermo-chemical LLVPs, and that the relative viscosity between the LLVPs and the ambient mantle influences their morphology [18, 27]. Two-dimensional simulations also suggest that changing subduction patterns affect the distribution of LLVP material in the lowermost mantle [26], but a 3D approach is necessary to fully understand the effect of Earth-like subduction patterns.

To investigate in 3-D the transport and accumulation of SOC in the mantle we use the mantle circulation code TERRA [28, 29] (Methods 6.1). A 3-D approach allows us to include Earth-like plate subduction history and perform geographically referenced comparisons between simulations and observations. We will estimate the shapes and locations of the LLVPs, how LLVPs develop over time, and map differences in their bulk composition (i.e., SOC enrichment) and age (i.e, most recent melting of SOC) to gain understanding of their long-term evolution.

2 Numerical simulations of LLVPs

We solve the governing equations of mantle convection under the Boussinesq approximation, with isothermal boundary conditions and a depth and temperature-dependent viscosity (Methods 6.1). Kinematic reconstructions of plate motions [30, 31] are used to constrain surface plate velocities and therefore the paleo-locations of subduction zones and spreading ridges over the past 1 Gyr. This long simulation time captures the cycle of oceanic crust segregation from the subducted lithosphere, descent through the mantle, accumulation of SOC at the CMB, and entrainment and replenishment [20, 21]. Oceanic crust is generated via a melting process [32–34] at mid-ocean ridges and plume heads, with the material recycled into the mantle in plate convergence zones (Methods 6.2). Bulk composition (C) is parameterised as a scalar which ordinarily varies between 0 and 1, with three principal lithologies prescribed in our model: harzburgite ($C = 0.0$), lherzolite ($C = 0.2$), and basalt ($C = 1.0$). For simplicity we use this terminology when referring to high pressure assemblages of these lithologies. The temperature and composition fields are converted to seismic velocities (Methods 6.3.1) and adjusted for the tomographic resolution to facilitate a comparison with S40RTS [35] (Methods 6.4).

We focus the discussion on the results of reference simulation RCY (Table 1). Simulation RCY features a radial viscosity profile of three layers (Supplementary Figure S1) with lateral variations in viscosity determined by temperature variations (Methods, 6.1). RCY predicts present-day accumulations of SOC in the lower mantle under the Pacific and Southern Ocean (Fig. 1h) and elevated temperatures in the lower mantle beneath the Pacific and southern Africa (Fig. 1g), where plumes are preferentially formed (Fig. 1a,d).

The low shear-wave velocity anomalies (δV_s) beneath Africa and the Pacific are in similar locations and have similar shapes as the LLVPs in S40RTS (Fig. 1c, f, i, Supplementary Figure S2). This is also evident from the strong positive correlation between the δV_s structure in RCY and S40RTS throughout the lower mantle up to spherical harmonic degree 4 (Supplementary Figure S3). Henceforth, we refer to these low δV_s structures as the simulated large low velocity provinces, or s-LLVPs, but we note that the LLVPs in S40RTS and the s-LLVPs in RCY are not exactly similar. The s-LLVPs in RCY are broader (Supplementary Figure S4), the Pacific s-LLVP is more spatially discontinuous (Fig. 1c, f, i), and the s-LLVP beneath Africa is connected to the Pacific s-LLVP at its southeastern tip. The shear-wave velocity reduction is slightly smaller than in model S40RTS, especially in the lowermost mantle (Supplementary Figure S4i, j).

The buoyancy number of SOC of 0.66 corresponds to a lower mantle excess density of +4.5% for basalt relative to the average mantle. This is slightly larger than estimates from mineral physics [36–38]. For a compressible mantle, this translates to a value of +2.1%, similar to recent calculations of the excess density of SOC in the lower mantle [36, 37].

Nine additional simulations (Table 1) explore the effects of the assumed buoyancy of SOC in the lower mantle (B=0.44 and B=0.22) [36–38], the mantle viscosity structure (visc2 and visc3) [39], the CMB temperature (CMB2800 and CMB2600) [40, 41], the effects of compressibility (COMP), the presence of dense primordial material at

Table 1 Table of model parameters, showing the buoyancy number, viscosity profile and CMB temperature used in each simulation. Note that most simulations are incompressible and an adiabatic contribution must be added to compare to Earth. Viscosity profiles are plotted in Supplementary Figure S1.

Name	Buoyancy Number of SOC	Viscosity Profile	T_{CMB} (K)	Primordial Layer Thickness (km)	Plate Model
RCY	0.66	visc1	3000	-	Müller et al (2022)
B=0.44	0.44	visc1	3000	-	Müller et al (2022)
B=0.22	0.22	visc1	3000	-	Müller et al (2022)
visc2	0.66	visc2	3000	-	Müller et al (2022)
visc3	0.66	visc3	3000	-	Müller et al (2022)
CMB2800	0.66	visc2	2800	-	Müller et al (2022)
CMB2600	0.66	visc2	2600	-	Müller et al (2022)
PRM	0.66	visc1	3000	150	Müller et al (2022)
COMP	0.66	visc1	4000	-	Müller et al (2022)
MER	0.66	visc1	3000	-	Merdith et al (2021)

the CMB (PRIM), and the choice of plate motion history (MER) [31]. With the exception of simulation visc2, all simulations have a total weighted layer correlation greater than 0.3 up to degree 8 ($p = 0.01$ from Becker and Boschi [42]) for depths greater than 1100 km (Supplementary Figure S5). Simulation MER has the lowest correlation to S40RTS through much of the lower mantle, which likely reflects differences in the plate motion reconstruction prior to 300 Ma.

3 Evolution, composition, density and age differences between s-LLVPs

To interrogate the African and Pacific s-LLVPs individually, we first isolate the low velocity regions using a K-means clustering technique applied to the filtered δV_s field (Methods 6.5). We then separate the African and Pacific regions based on a longitude cut-off. The differences in the radially averaged bulk composition, temperature, and V_s of the Pacific and African s-LLVPs in the lowermost 680 km of the mantle depend on the property considered. If measured by the depth-integrated areal extent of the s-LLVPs over each radial layer (Fig. 2d), the African s-LLVP is only 5% more voluminous than the Pacific s-LLVP (Fig. 2d). Their average temperature and shear-wave velocity (Fig. 2b–c) differ by up to only 3.9 and 0.18% respectively.

However, the difference in composition is large. Above 2700 km depth, the bulk composition of the African s-LLVP is similar to the mantle average value of $C = 0.2$ (Fig. 2a), increasing to $C = 0.35$ at the CMB. In contrast, the Pacific s-LLVP contains a broader range of compositions (Fig. 3a-c), and it is enriched in basalt compared to the average mantle by up to 53%. Basalt enrichment of the Pacific s-LLVP is accompanied by reduced harzburgite and lherzolite fractions, with the harzburgite fraction being particularly small in the lowermost mantle (Fig. 3a). The compositional disparity between the Pacific and African s-LLVPs occurs in all simulations, although the degree of enrichment in SOC varies. For instance, in simulations with different radial viscosity profiles in the lower mantle (Supplementary Figure S8), the Pacific s-LLVP is enriched by up to 58% and 25% compared to the African s-LLVP for simulations visc2 and

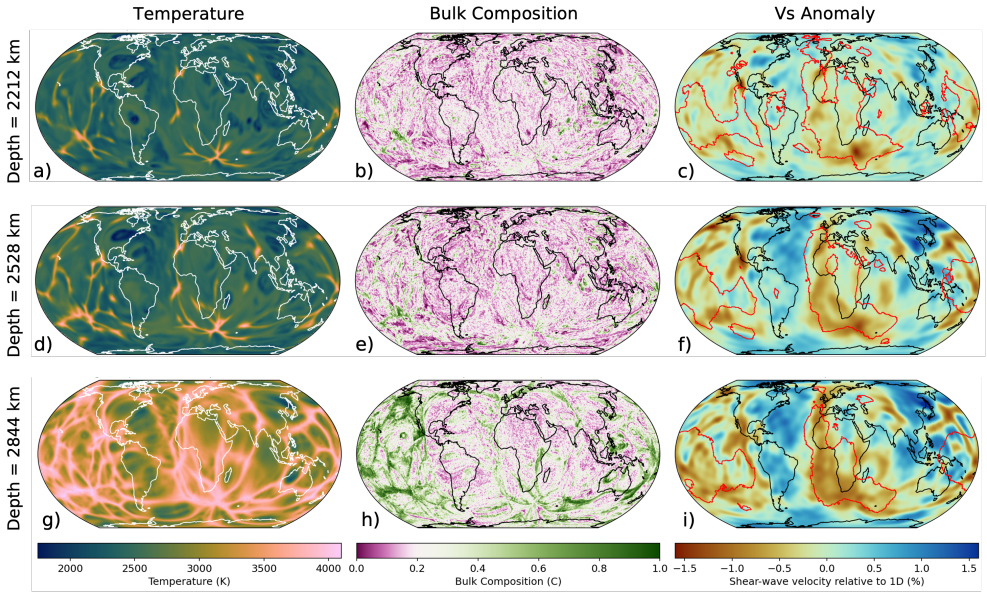

Fig. 1 Present day mantle structure predicted by simulation RCY showing temperature (a, d, g), bulk composition (b, e, h), and converted shear-wave speed filtered using the resolution of seismic tomography model S40RTS [35] (c, f, i) at 2212 km (top tow), 2528 km (middle row) and 2845 km (bottom row) depth. The colour scale for bulk composition is centred on $C = 0.2$, which is the average composition for the mantle, with purple colours indicating depleted material and green colours indicating enriched material. The seismic velocities are obtained by assuming that the bulk composition C of the tracer fields represents a mechanical mixture of the 3 principal lithologies (Methods 6.3). Red lines plotted on top of shear-wave velocity maps outline the margins of the LLVPs in a "vote map" of 18 shear wave tomography models [43, 44], indicating where at least 5 models are in agreement.

visc3 respectively. At lower CMB temperatures, the Pacific s-LLVP is also enriched relative to the African s-LLVP (Supplementary Figure S9), and the same difference is observed when using a compressible equation of state (Supplementary Figures S10, S3j-l). Even when using a plate reconstruction model that differs significantly before $\sim$ 300 Ma (Merdith et al. [31], case 'MER', Table 1), we find that the Pacific s-LLVP is strongly enriched in SOC compared to the African s-LLVP (Supplementary Figure S10e). This implies that SOC enrichment of the Pacific s-LLVP is a robust result in our simulations and indicates that the circum-Pacific downwellings during the past 300 Myr strongly influence the distribution of SOC in the lower mantle [7, 23].

The melting age, defined as the average time since particles in a cell underwent melting, offers an insight into the reworking history of s-LLVPs (Fig. 3f). For the African s-LLVP, the melting age distribution is mostly skewed towards older ages (high melting age), with greater proportions of younger (low melting age) material in the lowermost $\sim$150 km of the mantle. This implies that much of the constituent material of the African s-LLVP has been sequestered in the lower mantle for $\sim$1 Gyr. Conversely, the melting age distribution for the Pacific s-LLVP is a Gaussian centered

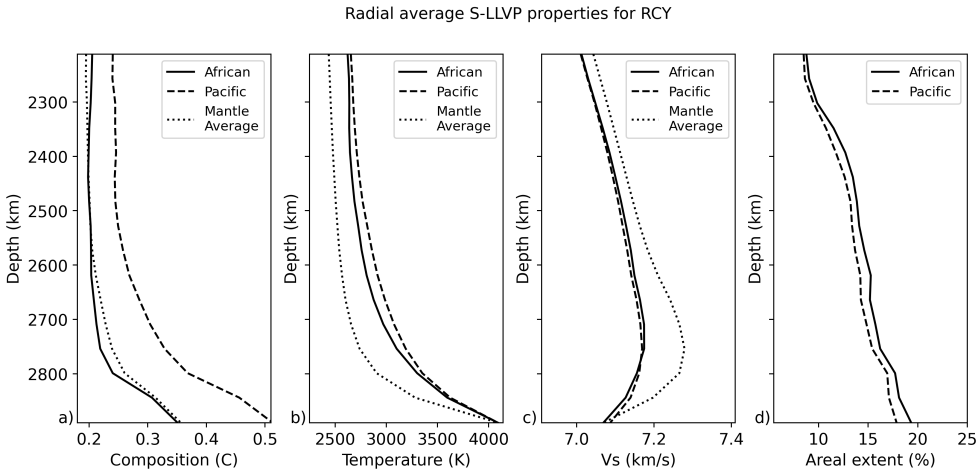

Fig. 2 Radial average of present day s-LLVP properties in simulation RCY, showing (a) bulk composition, (b) temperature, (c) predicted absolute shear-wave velocity (unfiltered) in the African s-LLVP (solid lines) and Pacific s-LLVP (dashed lines) and (d) the areal extent of each s-LLVP in each radial layer. A theoretical adiabat (Supplementary Figure S6) has been added to the temperature field to account for model incompressibility.

on an age of 750 Myr down to ∼2600 km depth. At greater depths the melting ages are skewed to lower values (Fig. 3f). This suggests that on average the constituent material of the African s-LLVP is older than in the Pacific s-LLVP, and that there has been a large and recent influx of young SOC into the base of the Pacific s-LLVP. This may indicate that the African s-LLVP was formed prior to the Pacific s-LLVP or that in recent times young SOC accumulates preferentially in the Pacific s-LLVP.

Simulation RCY predicts how the subducted oceanic crust accumulates (Figure 4) and how it has been redistributed by mantle circulation over the past 1 Gyr. A large volume of SOC converges in the northern hemisphere from the beginning of the simulation until 800 Ma. Between 800 and 600 Ma, this volume begins to split while new SOC enters the lower mantle from subduction primarily at mid to low latitudes. From 600 to 400 Ma, the subduction zones migrate into a circum-planetary girdle and the accompanying downwellings push SOC away from these regions. At 300 Ma, strong lateral flow in the lowermost mantle brings SOC under the present-day Pacific region, while weak flow beneath present-day Africa allows SOC accumulations to move slowly south (Figure 4, Supplementary Video SV1). From 200 Ma to present day, SOC continues to be added beneath the Pacific region, replacing the material that was lost through entrainment by persistent plumes, as implied by the melting age distribution (Fig. 3f). A steady rate of replenishment of young SOC [20, 21] therefore enables the Pacific s-LLVP to be maintained. Accumulations of SOC beneath present-day Africa continue to migrate south and are almost completely removed from the lowermost mantle by a strong plume that develops in the Southern Indian ocean. The entrained SOC is replaced by relatively old, depleted and well-mixed material compared to that which replenishes the Pacific s-LLVP (Figs. 4,5).

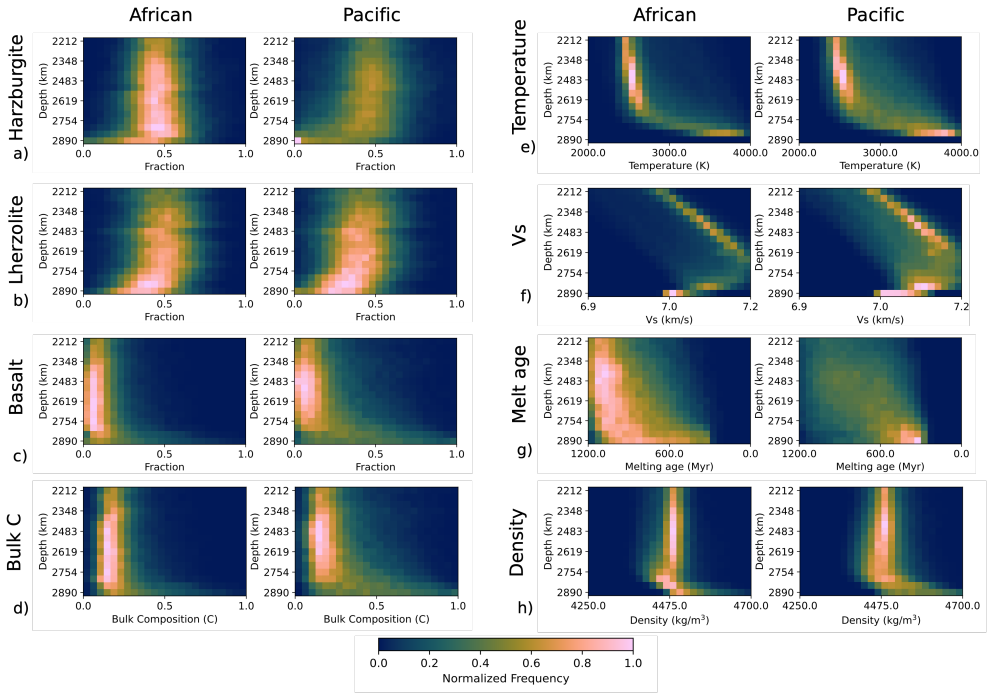

Fig. 3 Histograms for bulk composition, temperature, shear-wave velocity (V_s, unfiltered), melting age and density of the African (left plot in each panel) and Pacific (right plot in each panel) s-LLVPs. The proportions of (a) harzburgite, (b) lherzolite, and (c) basalt together define the d) bulk composition. We also plot the (e) temperature, (f) predicted absolute shear-wave velocity, (g) melting age and (h) density distributions. Due to the isothermal boundary condition of the simulation at the CMB, the temperature is not plotted at this depth.

In simulation RCY, the lower mantle excess density of basalt relative to the average composition (+4.5%) is greater than current mineral physics estimates [36–38]. However, we find the same trend between the African and Pacific s-LLVP for simulations with buoyancy numbers that correspond to excess densities of +3.0% ($B = 0.44$, Supplementary Figure S7e) and +1.5% ($B = 0.44$, Supplementary Figure S7a), albeit with reduced basalt enrichment in the lowermost mantle. Due to a relatively high concentration of basaltic material, the Pacific s-LLVP is denser than the African s-LLVP (Fig. 3h), as SOC is expected to be denser relative to the ambient composition of the lowermost mantle. This intrinsic density may be a controlling factor on LLVP height, with the African LLVP being more buoyant and therefore more unstable [45]. Our results imply that the compositional, intrinsic density and height differences between the two LLVPs are a natural consequence of time-varying mantle flow and different time-integrated replenishment rates.

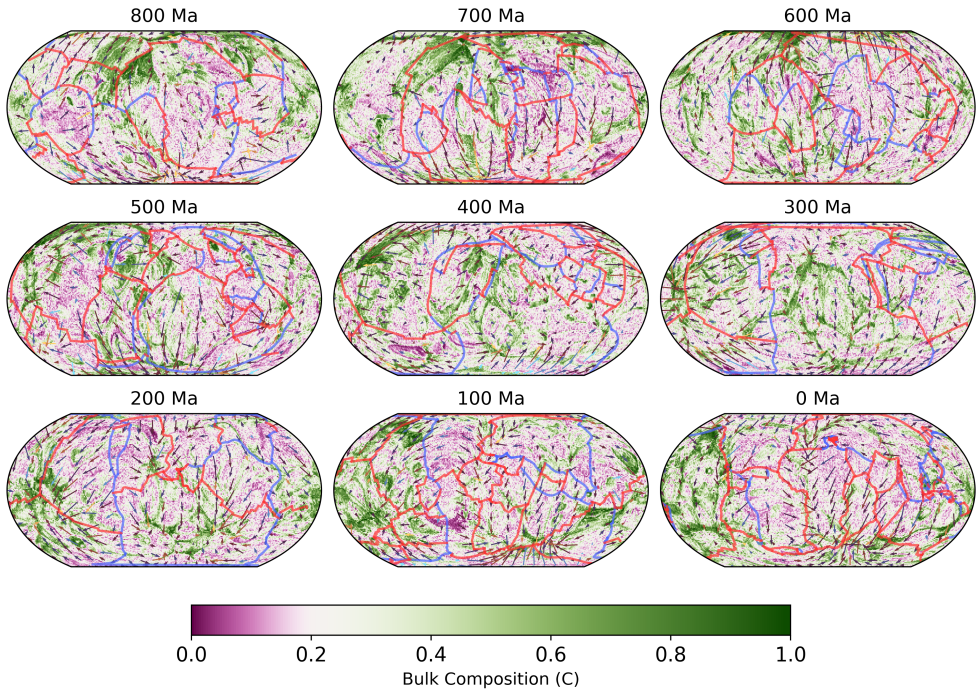

Fig. 4 Time evolution of mantle composition, illustrated by depth slices at 2844 km depth at 100 Myr intervals from 800 Ma to present day for simulation RCY, coloured by bulk composition. Red lines indicate ridge and transform boundaries and blue lines indicate subduction zones, as defined by the plate reconstruction used for the surface boundary condition [30]. Arrows indicate the direction and magnitude of horizontal flow at 2844 km depth, coloured by the radial velocity with cool colours indicating downward flow (toward CMB) and hot colours indicating upward flow (toward surface).

4 Discussion

Our 3-D simulations of the production and circulation of oceanic crust using models of plate-motion history from the past billion years predict that (SOC) accumulates into two antipodal piles in the lower mantle beneath Africa and the Pacific akin to the two large low velocity provinces (LLVPs) imaged seismically (Fig. 4) [see also 6, 7, 23]. Combined, the areal extent of the simulated s-LLVPs in RCY increases from 17% at 2212 km depth to 37% at the CMB (Fig. 2), making them laterally more extensive than seismically imaged LLVPs. This is likely due to the imperfect representation of historic subduction zones in the plate reconstruction model, imperfect lower mantle viscosities, and the effects of composition-dependent viscosity. The latter would affect the stability of basal mantle structures [46], potentially making it easier for downwellings to sculpt the s-LLVPs and decreasing their footprint at the CMB.

Our simulations indicate that persistent plumes in the Pacific induced a mantle flow pattern at the CMB that pulled in newly subducted slabs (Supplementary Video SV1, Fig. 4, 6). This resulted in enrichment of the Pacific s-LLVP in young SOC (Fig. 5).

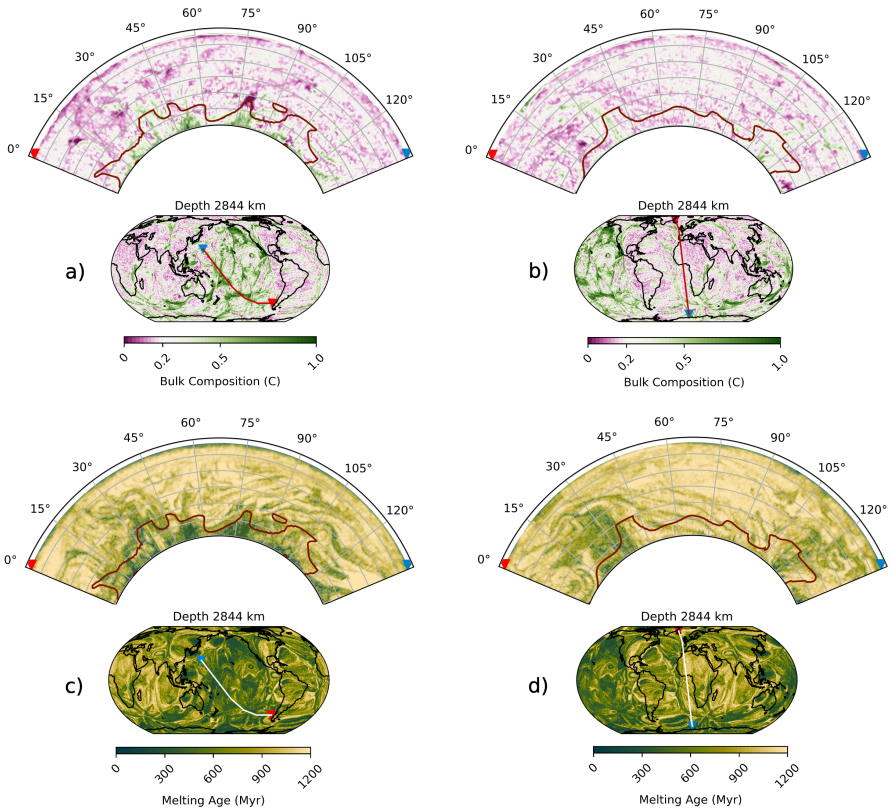

Fig. 5 Cross sections through the present-day mantle as simulated by simulation RCY, coloured by a,b) bulk composition and c,d) melting age (i.e. average time since last melting). The inset map shows the location of the cross sections with red and blue triangles indicating the extend of the cross section. Cross section locations have been chosen to pass through a,c) the Pacific s-LLVP and b,d) the African s-LLVP. Outlines of the s-LLVPs are shown in red up to 1000 km above the CMB.

In contrast, in the last ∼300 Myr the African s-LLVP is replenished with older, better mixed material with a bulk composition closer to mantle average compared to the Pacific s-LLVP (Figs. 4,5).

The enrichment in basalt of the Pacific s-LLVP appears inconsistent with recent geochemical inferences that enriched mantle type intra-plate hotspots are more commonly associated with the African LLVP [47]. However, the difference in mean bulk composition of plumes associated with the two s-LLVPs is surprisingly low in RCY (Supplementary Figure S11), given the compositional difference between the two s-LLVPs (Fig. 2a). This may be because plumes form and preferentially entrain material from the edges of the s-LLVPs [48]. The mean plume composition of the two domains also converges towards the surface, possibly due to increased mixing at shallower

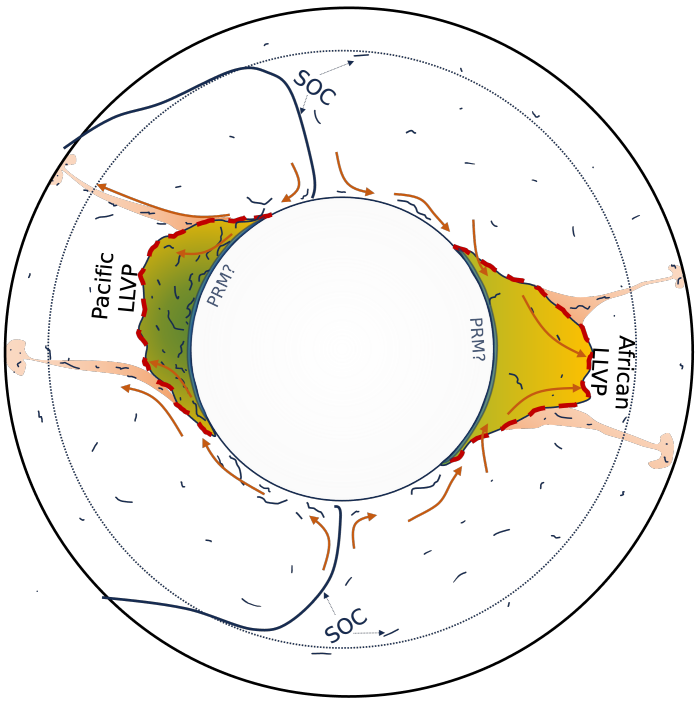

Fig. 6 Schematic diagram for the proposed mechanisms that sustain the Pacific and African LLVPs over the past $\sim$ 300 Myr. Dark blue strands represent SOC with orange arrows indicating the flow of material in and out of the LLVPs. The Pacific LLVP is fed at its base by young (green) SOC , while the African LLVP consists of well-mixed, older (yellow) material. Our simulations do not rule out the possibility of a thin layer of dense primordial material (PRM) at the base of the LLVPs.

depths. It should be noted that our simulations do not include recycling of continental crust or marine sediments, so we do not expect to explain all of the compositional complexities observed in mantle plumes.

Some studies suggest that the African LLVP reaches up to 550km higher above the CMB than its counterpart [9, 10] although the exact height difference is subject to the tomographic model and velocity contour used to define the LLVPs. Contrasting internal buoyancy between the LLVPs caused by different compositions [45] and distinct formation histories has been suggested as a reason for the height difference. Geochemical evidence from an analysis of plume lavas associated with the two regions [47] appears to support a compositional difference between the African and Pacific LLVPs. However, others suggest that apparent geochemical differences are due to sampling bias and argue that there is no significant difference between the isotopic composition of plumes originating from the African and Pacific LLVPs [49], with height differences between the LLVPs being attributed to limited seismic resolution [50, 51] and uncertain image interpretations. Our simulations suggest that compositional differences between the LLVPs are expected to naturally arise due to the historic pattern of subduction of oceanic crust. Consequently the internal density of structure may differ between the two LLVPs (Fig. 3h), contributing to their height difference.

Despite the strong compositional contrast between the African and Pacific s-LLVPs (Figs. 2a, 3a-c), their predicted radially averaged temperature and V_s differ by only 3.9% and 0.18% respectively (Fig2b,c). This is because of the dominant effect of temperature relative to composition on the V_s of lower mantle minerals. While this arises from the mineral physics dataset used in our study (Methods 6.3.2, Supplementary Figure S12), we believe the conclusion that the temperature effect dominates that of the composition holds up in general [52].

Recent work suggests that in order to fit multiple robust geophysical constraints, such as dynamic topography, the geoid and normal-mode frequency variations, LLVPs may contain denser than average material at their base [53], with chondrite-enriched basalt (CEB) proposed as a possible composition for this material [12]. Since our simulation is limited to the past billion years for which plate reconstruction models are available, it is not feasible to incorporate the recycling of CEB during the Hadean in our simulations. However, if we start a simulation at 1.2 Ga with a 150 km thick layer of dense material at the base of the mantle with a unique ($C = 2.0$) composition (simulation PRM, Table 3), we find that the Pacific s-LLVP is still more enriched in SOC than the African s-LLVP (Supplementary Figure S13c), while it is additionally enriched in the primordial component (Supplementary Figure S13d). At the base of the mantle, this amplifies δV_s, making it similar to that observed in S40RTS (Supplementary Figure S4i), compared to simulation RCY which underestimates the shear-wave reduction (Supplementary Figure S4a-f). However, at shallower depths the velocity reduction in PRM is larger than observed in S40RTS (Supplementary Figure S4g,h). Given the more Earth-like shear-wave velocity reductions that can be achieved at the base of the s-LLVPs when they are enriched in CEB, we cannot rule out that primordial, chemically distinct material is present at the base of LLVPs, possibly buried and trapped at the base of the mantle by SOC [54, 55].

The assumption of an incompressible mantle may contribute to the relatively small reduction in shear-wave velocity of the s-LLVPs compared to tomographic observations. To account for compressibility of the mantle, we add a theoretical adiabat to the simulations, scaling the temperature field at each depth by the same value. While this process leads to 1D mantle temperature profile with a more Earth-like thermal gradient, the temperature range at each depth is unchanged. This may lead to reduced lateral variation in shear-wave velocity compared to a compressible mantle circulation simulation because a compressible mantle could retain cooler slabs relative to those in the temperature adjusted incompressible model. However, our tests using a compressible mantle circulation simulation (COMP), indicate that the velocity reductions in the s-LLVPs are not significantly different from those in the reference simulation RCY (Supplementary Figure S4d,h,l). Like RCY, the compressible simulation produces a Pacific s-LLVP that is enriched in SOC compared to the African s-LLVP (Supplementary Figure S10a). A further source of error in estimating seismic velocities stems from the choice of the thermodynamic database. Although we have used a recent version of an established database [56], this does not include the iron spin transition in the lower mantle [57–59] and it differs from an earlier, widely-used version [60]. The significant changes in thermodynamic databases reflect the fact that the determination

of seismic velocities at lower mantle pressures and temperature remains difficult due to experimental challenges under extreme conditions.

5 Conclusions

Our models of mantle circulation over the past billion years demonstrate that LLVPs can naturally develop as a consequence of recycling oceanic crust. The African and Pacific LLVPs have similar elevated temperatures and hence similar reduced shear wave speeds since temperature affect V_s more than composition. However, the Pacific and African LLVP evolve differently and have different compositions as a consequence of the plate motion history from the past 1 Gyr. Melting ages indicate that the material in the African LLVP is older and better mixed than in the Pacific LLVP which has been replenished by subducted oceanic crust during the past 300 Myr. Compared to the Pacific LLVP, the African LLVP is less enriched in basaltic rock and therefore less dense and more buoyant, supporting the idea that the African LLVP can rise higher into the mantle than the Pacific LLVP. Further studies should investigate the role of primordial material at the base of LLVPs on their dynamical evolution.

6 Methods

6.1 Dynamic simulations

The simulations presented in this study have been run using the three-dimensional mantle convection code, TERRA [28, 29, 61, 62]. Under the Boussinesq approximation and assuming an incompressible mantle [63], the equations for conservation of mass, momentum and energy are:

$$\nabla \cdot \boldsymbol{u} = 0 \tag{1}$$

$$\nabla \cdot \left(\eta \left\{\nabla \boldsymbol{u} + (\nabla \boldsymbol{u})^T\right\}\right) - \nabla p = \boldsymbol{g}\,\alpha\,\rho_0\,(\delta T - C\,B\,\Delta T) \tag{2}$$

$$\rho_0\,C_p \left(\frac{\partial T}{\partial t} + \mathbf{u}\cdot\nabla T\right) - k\,\nabla^2 T - H = 0 \tag{3}$$

respectively, where $\boldsymbol{u}$ is fluid velocity, η is dynamic viscosity, T is temperature, p is dynamic pressure, $\boldsymbol{g}$ is the acceleration due to gravity, α is the coefficient of thermal expansion, ρ_0 is the reference density, C is the bulk composition (ranging between 0 and 1), B is the buoyancy number, ΔT is the temperature contrast across the mantle, t is time, C_p is the specific heat capacity constant pressure, k is thermal conductivity, H is the radiogenic heat production per unit volume and $\delta t = (T - T_{ref})$ where T_{ref} is our reference temperature profile. The buoyancy number is defined as:

$$B = \frac{\Delta\rho_b}{\alpha\rho_0\Delta T} \tag{4}$$

where $\Delta\rho_b$ is the intrinsic density difference between basalt ($C = 1$) and lherzolite ($C = 0.2$, average mantle) in the lower mantle. The advection of bulk composition is described as:

$$\frac{\partial C}{\partial t} = -\nabla \cdot (C\mathbf{u}) + S \tag{5}$$

Table 2 Common parameters to all simulations and their values. Reference viscosity is equal to the viscosity of the upper mantle.

Symbol	Parameter	Value	Unit
T_s	Surface temperature	300	K
η_0	Reference viscosity	$4\text{x}10^{21}$	$Pa\,s$
ρ_0	Reference density	4500	$kg\,m^{-3}$
k	Thermal conductivity	4	$W\,m^{-1}K^{-1}$
α	Thermal expansivity	$2.5\text{x}10^{-5}$	K^{-1}
C_p	Specific heat capacity	1100	$J\,kg^{-1}K^{-1}$

as in van Heck et al. [32], where S represents melting described in detail below in section 6.2.3. The model parameters and parameter values are listed in Table 1 and Table 2.

The model domain is discretised into 65 concentric layers, each composed of a regular icosahedron that is projected onto a sphere, with a radial spacing of ∼45 km. At each radial layer, the icosahedron is sub-divided, leading to an average lateral resolution at the surface and CMB of ∼60 km and ∼33 km respectively [28]. While such a resolution is sufficient to resolve long-wavelength mantle features, it is too large to resolve the ∼6-7 km thick oceanic crust. The oceanic crust in our models is defined by bulk composition, which is tracked on particles, thus providing a sub-grid resolution. To estimate the thickness of the oceanic crust we look at the fraction of particles (Methods 6.2) in the oceanic domain that have a bulk composition of $C = 1.0$ in the oceanic basins. As oceanic crust is by definition basaltic, at least more than 50% of particles at a given depth must be basaltic ($C = 1.0$). Using this definition, we find the oceanic crust to have an average thickness of 10 km in our simulations (Supplementary Figure S14). This includes any unusually thick areas of crust that could be likened to plateaus and seamounts. This oceanic crust is expected to largely follow the trajectory of the subducting slab as it descends into the mantle due to viscous coupling [64].

From an initial temperature distribution, the simulation is allowed to evolve for 2 Gyr with a free-slip surface boundary condition in a pre-conditioning phase. This ensures that any signal from the initial thermal structure is removed. We then run the conditioning phase whereby the first stage of the plate motion reconstruction [30] acts as the surface velocity boundary condition. This is applied for 200 Myr in order to introduce temperature, velocity and compositional structures into the mantle that reflect the overlying plate assemblage. Finally, each simulation is run forwards in time from 1000 Ma to the present day with surface velocities updated every 1 Myr.

To avoid numerical instabilities and artefacts, the reference viscosity used in our simulations (Table 2), is higher than what is expected for Earth's upper mantle by approximately a factor of 4. Consequently, the RMS surface velocities during the pre-conditioning phase of the simulations (∼2.5 cm/yr), prior to plate velocities being imposed, are about 1/2 of what is estimated for the present day RMS surface velocity for plates on Earth [30]. Therefore, we apply a scaling factor of 1/2 to the reconstructed plate velocities so that they better match the flow velocities in our simulations, i.e. the reconstructed plate velocities are reduced by 50%. To compensate for the reduced surface velocities and to maintain the correct volume flux of material through ridges

and trenches, we must then apply a scaling factor of 2 to the model time t [65]. This gives rise to an important distinction between 'model time' and 'Earth time'. Throughout this work we quote time as Earth time when it is directly related to geological time, whereas the model time is larger by a factor of 2 (the time scaling factor).

Viscosity in the simulations depends on depth and temperature according to:

$$\eta = \eta_z \exp((z' V_a) - (E_a T')) \tag{6}$$

where η is the viscosity, η_z is the reference viscosity (η_0) multiplied by the radial viscosity factor (Supplementary Figure S1) at depth z, z' is the non-dimensional depth, V_a=1.0 and E_a=2.0 are non-dimensional constants that control the sensitivity of viscosity to depth and temperature, and T' is the non-dimensional temperature. Depth is non-dimensionalised by $z' = z/h$, where h is the thickness of the mantle. Temperature is non-dimensionalised by $T' = (T - T_s)/(T_c - Ts)$, where T is the mantle temperature at a given point, T_s is the temperature of the surface boundary, and T_c is the temperature of the lower boundary at the CMB.

All profiles for η_z feature a strong lithosphere with a thickness of 135 km, a weak upper mantle with viscosity equal to the reference value, and a 30× viscosity jump across the 660-km discontinuity [66]. In the lower mantle, we use three profiles (Supplementary Figure S1) to explore different causes for an increase of the viscosity with depth, assuming it to be either due to increasing bridgmanite concentrations or increasing strength of ferropericlase with depth. In the lowermost mantle the radial viscosity profile also features a reduction to approximate the decrease in viscosity associated with the lower mantle bridgmanite to post-perovskite phase transition [22] and the CMB thermal boundary layer. The impact of the latter is also accommodated by the temperature dependence of the viscosity.

6.2 Particles

6.2.1 Bulk composition parameterization

We use tracer particles to track bulk composition and abundance of heat producing elements. Simplified bulk composition is stored as a value (C) that varies between $C = 0.0$, representing completely depleted material (harzburgite), and $C = 1.0$, representing completely enriched material (basalt), while we consider the bulk silicate Earth composition to be lherzolite. Together, these three compositions represent the characteristic lithologies of the mantle. They are each assigned a bulk composition composed of six major oxides (Table 3), with proportions chosen to fit results from Baker and Beckett [67] for harzburgite, Walter [68] for lherzolite and White and Klein [69] for basalt. To determine the C-value of lherzolite, we find the best fit vector between the major element mass proportions of harzburgite, lherzolite and basalt, finding this to be $C = 0.2$. Different choices for the bulk composition of basalt, harzburgite and lherzolite result in slightly different values of C (ca. 0.18–0.21 mass fraction basalt).

Table 3 Assumed molar composition for our three standard characteristic lithologies (harzburgite, lherzolite, basalt) as well as the 'primitive' composition (CEB).

	Harzburgite	**Lherzolite**	**Basalt**	**CEB**
SiO2	36.184	38.819	52.298	48.47
MgO	56.559	49.894	15.812	20.00
FeO	5.954	6.145	7.121	11.28
CaO	0.889	2.874	13.027	10.59
Al2O3	0.492	1.963	9.489	11.28
Na2O	0.001	0.367	2.244	1.50

At the start of the pre-conditioning phase, each cell is initialised with 10 particles, with $1 \times C = 1.0$ particle, $5 \times C = 0.2$ particles and $4 \times C = 0.0$ particles, giving a mean mantle composition of $C = 0.2$.

6.2.2 Solid phase transitions in the geodynamic simulations

In our geodynamic simulations, we use a simplified parameterization of the phase transitions in the olivine system, which occur at 410 and 660 km depth (Table 4). This parameterization allows us to reproduce some of the behaviour associated with these discontinuities [33, 70]. The depth and bulk composition of particles affects the density field, which is quantified by the buoyancy number (Equation 4). We vary the buoyancy number in our simulations (Table 1) to investigate the effect of different intrinsic densities of SOC [21], estimates of which vary between 0.5 and 5% more dense than average mantle [36, 38, 71].

6.2.3 Melting in the geodynamic simulations

A linear solidus, dependent on depth (z) and bulk composition, controls melting in the simulations [21, 32, 33]:

$$T_{\text{solidus}}(z, C) = T_{\text{meltsurf}} + zT_{\text{meltslope}} + (1 - C)T_{\text{meltcomp}} \tag{7}$$

where $T_{\text{meltsurf}} = 1200$ K is the melting temperature of basalt ($C = 1$) at the surface, $T_{\text{meltslope}} = 2.5$ K km^{-1} is the gradient of the solidus and $T_{\text{meltcomp}} = 500$ K is the temperature difference between the solidi of basalt ($C = 1$) and harzburgite ($C = 0$). At each time step, we check whether particles in the uppermost 135 km have crossed their solidus. If this is the case, the melting particle has its bulk composition reduced so that it plots on the solidus for the particle's temperature and pressure until it cannot be further depleted ($C = 0$). Particles in the shallowest cell vertically above the melt producing particle are enriched with the produced melt first, assuming instantaneous melt migration. If all particles in the shallowest cell are completely enriched, subsequently particles in the cell below are checked to see whether they can be enriched by the melt. Full details of this melting process in the dynamic simulations can be found in refs. [21, 32, 34].

Table 4 Olivine phase change parameters for an assumed composition with 67% $(Mg, Fe)_2\,SiO_4$.

Depth (km)	$\Delta\rho\,\mathrm{kg\,m^{-3}}$	Clapeyron slope $\mathrm{MPa\,K^{-1}}$
410	230	2.25
660	380	-1.5

6.3 Seismic properties

6.3.1 Converting from simulation to seismic properties

We convert the pressure, temperature and composition of our simulations to seismic properties using look-up tables for each of the characteristic lithologies. Due to the incompressible equation of state used in our simulations, we add a theoretical adiabat to the simulated temperature field before performing this conversion. We use the thermodynamic data set of [56], implemented in the Perple_X software [72] to generate tables for density and effective isotropic seismic properties for each lithology in pressure - temperature space. Attenuation is accounted for using model Q7g [73, 74]. The thermodynamic data set includes all major mantle phase transitions, but does not include the spin transition in ferropericlase, nor the second order phase transition in stishovite. Although these may reduce seismic velocities in the lower mantle, mineral physics studies indicate that the effect on the shear-wave velocity is small [59].

As the bulk composition in our simulation is tracked using only a single parameter C, it is not possible to differentiate between mechanical and equillibrated mixtures of different compositions. We therefore make a pragmatic decision for how to convert C to lithology. An important requirement is that primitive mantle is modelled as pure lherzolite, not as a mechanical mixture of basalt and harzburgite. Therefore, we model particles with a bulk composition between $C = 0.0$ and $C = 0.2$ as a mechanical mixture [75] of harzburgite and lherzolite, and particles with a bulk composition between $C = 0.2$ and $C = 1.0$ as a mechanical mixture of lherzolite and basalt. The relative proportions of each characteristic lithology are interpolated from the particles to the grid so that at each grid point we have information on the relative proportions of each of the three lithologies. Seismic properties at the grid point are then calculated by taking the harmonic mean of the properties for each lithology at the temperature and pressure of the grid point, weighted by the relative proportions of each lithology. Although our one-parameter compositional tracking and simplified geodynamic approach to phase transitions do not capture the full effects of chemical variation in the mantle, our post-processing approach is highly efficient and facilitates a detailed exploration of model parameters such as buoyancy number (excess density of SOC), independently from the thermodynamic model. This also allows us to investigate the choice of different assumed compositions independently of the geodynamic model.

6.3.2 The dominant effect of temperature on V_s

For the assumed molar compositions of the characteristic lithologies (Table 3), the predicted δV_s between lherzolite and harzburgite is small (Supplementary Figures S12a,b,d, S15) at lower mantle pressures. This is because both lherzolite and harzburgite are silica-undersaturated and are dominated by bridgmanite and ferropericlase.

The V_s of basalt varies more strongly with temperature and pressure (Supplementary Figure S12c). Between 80 and 95 GPa, the V_s of basalt is about 0.1 km/s higher than that of lherzolite (Supplementary Figure S12e) and harzburgite (Supplementary Figure S12f), but with increasing pressure the V_s of basalt becomes lower than lherzolite and harzburgite across an increasingly wide temperature range. Nonetheless, the average difference in absolute V_s between harzburgite and basalt is just 0.07 km/s (about 1%). However, within the temperature range relevant to the s-LLVPs ($2200 - 4300K$, Fig. 3d), the mean of the differences between the maximum and minimum V_s at each 0.1 GPa pressure point between 80 and 140 GPa is 0.42 km/s for harzburgite and 0.40 km/s for lherzolite and basalt, i.e. about 5% variation.

As such, velocity variations are primarily determined by temperature variations in the mantle since the 5% variations in V_s due to temperature are greater than the 1% variations arising from compositional differences. The δV_s of the two s-LLVPs is thus comparable because they are both similarly hot compared to the ambient mantle [76, 77] (Fig.2b). Compositional differences (Figs.3a-c,2a) are undetectable seismically (Fig.2c), especially if the post-perovskite transformation is suppressed (Supplementary Figure S16). Note that the precise details of the post-perovskite transition remain debated.

6.4 Filtering

In order to quantitatively compare the numerical simulations to seismic tomography, we follow the approach of [50], thus accounting for the limited tomographic resolution. We choose to compare our simulations to seismic tomography model S40RTS as it includes good coverage in the lower mantle and the resolution matrix is readily available, which is essential for filtering the simulation results. The maps of simulated shear wave velocity variations in the mantle are first re-parameterized to spherical harmonic coefficients up to degree 40 and the same 21 radial splines as in model S40RTS. We then apply the S40RTS resolution matrix that describes how the tomographic resolution varies spatially due to the non-uniform seismic data coverage and applied model damping. The tomographic filter smooths the seismic velocity variations and suppresses amplitudes, but makes our predictions based on the simulation directly comparable with S40RTS, for example in Fig. 1 and Supplementary Figure S4, which show the filtered δV_s field.

We compute the correlation between the geodynamic model and the seismic tomography model (Supplementary Figure S3) directly using their spherical harmonic expansions. Suppose that for degree l and order m, the coefficients of the geodynamic model are $\{a_{lm}, b_{lm}\}$ and for the seismic tomography model they are $\{c_{lm}, d_{lm}\}$. The depth-dependent degree correlation between the two models is then given by [42, 78]:

$$r^l(z) = \frac{\sum_{m=0}^{l} (a_{dlm} c_{dlm} + b_{dlm} d_{lm})}{\sqrt{\sum_{m=0}^{l} (a_{lm}^2 + b_{lm}^2)} \sqrt{\sum_{m=0}^{l} (c_{lm}^2 + d_{lm}^2)}}, \tag{8}$$

where we have omitted the depth dependence of a_{lm}, b_{lm}, c_{lm} and d_{lm}. We further calculate the total weighted layer correlation up to degree l_{max} ($r^{tot}_{l_{\max}}$) using:

$$r^{tot}_{l_{\max}} = \frac{\sum_{l=1}^{l_{\max}} \sum_{m=0}^{l} (a_{lm}c_{lm} + b_{lm}d_{lm})}{\sqrt{\sum_{l=1}^{l_{\max}} \sum_{m=0}^{l} (a_{lm}^2 + b_{lm}^2)} \sqrt{\sum_{l=1}^{l_{\max}} \sum_{m=0}^{l} (c_{lm}^2 + d_{lm}^2)}}. \quad (9)$$

6.5 Identifying low velocity domains in our simulations

To identify low velocity domains in the filtered V_s field predicted from our simulations, we use a K-means clustering algorithm [79]. We apply this to the filtered δV_s field at depths between 2212 - 2890 km depth to split the field into three clusters. The points in the 'low' cluster comprise the simulated large-low-velocity-provinces (s-LLVPs). We separate this low cluster into the African and Pacific domains based on their longitude, where points in the Pacific domain have longitude $> 140°$ and $< -50°$. The geographic positions of these points in the model domain are then used to mask the model output fields to extract data only for points within the Pacific, African or both s-LLVPs (Supplementary Figure S2).

Acknowledgments

This work was supported by the NERC Large Grant Mantle Circulation Constrained (MC2): A multidisciplinary 4D Earth framework for understanding mantle upwellings (Grant NE/T012633/1). P.K. acknowledges support from a Royal Society University Research Fellowship (URF\1\180377). Numerical simulations were conducted on ARCHER2, the UK's national high-performance supercomputer. In our figures we make use of perceptually uniform colourmaps [80]. Post-processing and figure creation was aided by the use of Python package 'terratools' (https://doi.org/10.5281/zenodo.11506398). This is Cardiff EARTH CRediT Contribution 30. For the purpose of open access, the author has applied a CC BY public copyright licence to any Author Accepted Manuscript version arising.

Funding

This work was supported by NERC grant number NE/T012633/1 and Royal Society grant URF\1\180377.

Competing Interests

The authors declare no competing interests

Data availability

Simulation outputs for this study can be accessed at 10.5281/zenodo.13644719.

Code availabilty

The code TERRA used in this study is not freely available as the code predates open-source licensing. As such we do not have the rights to release all parts of the code, however code pieces which have been implemented for this study are available at 10.5281/zenodo.13644719 along with code for reproducing analysis carried out in this study. We also make use of the terratools package (10.5281/zenodo.11506398) for the analysis of simulation results. The Perple_X code to generate mineral physics lookup tables [72] is available at www.perplex.ethz.ch/. The code used for tomographic filtering of model results [50] can be requested viawww.earth.ox.ac.uk/∼niv4152/downloads_filtering.html.

Authors contributions

JP: Conceptualisation, methodology, software, validation, formal analysis, investigation, data curation, writing (original draft), writing (review & editing), visualisation **HD**: Conceptualisation, resources, writing (review & editing), supervision, project administration, validation, funding acquisition **PK**: Software, writing (review & editing), validation, funding acquisition **JR**: Software, writing (review & editing) **RM**: Software, writing (review & editing).

References

[1] Ritsema, J., Lekić, V.: Heterogeneity of seismic wave velocity in earth's mantle. Annual Review of Earth and Planetary Sciences **48**(1), 377–401 (2020) https://doi.org/10.1146/annurev-earth-082119-065909

[2] Li, X.-D., Romanowicz, B.: Global mantle shear velocity model developed using nonlinear asymptotic coupling theory. Journal of Geophysical Research: Solid Earth **101**(B10), 22245–22272 (1996) https://doi.org/10.1029/96JB01306 . _eprint: https://onlinelibrary.wiley.com/doi/pdf/10.1029/96JB01306. Accessed 2023-03-09

[3] Garnero, E.J., McNamara, A.K., Shim, S.-H.: Continent-sized anomalous zones with low seismic velocity at the base of Earth's mantle. Nature Geoscience **9**(7), 481–489 (2016) https://doi.org/10.1038/ngeo2733 . Number: 7 Publisher: Nature Publishing Group. Accessed 2023-03-09

[4] Davies, D.R., Goes, S., Lau, H.C.P.: Thermally Dominated Deep Mantle LLSVPs: A Review. In: Khan, A., Deschamps, F. (eds.) The Earth's Heterogeneous Mantle: A Geophysical, Geodynamical, and Geochemical Perspective, pp. 441–477. Springer, Cham (2015). https://doi.org/10.1007/978-3-319-15627-9_14

[5] Bower, D.J., Gurnis, M., Seton, M.: Lower mantle structure from paleogeographically constrained dynamic Earth models. Geochemistry, Geophysics, Geosystems **14**(1), 44–63 (2013) https://doi.org/10.1029/2012GC004267 . _eprint: https://onlinelibrary.wiley.com/doi/pdf/10.1029/2012GC004267. Accessed 2023-03-08

[6] Cao, X., Flament, N., Bodur, .F., Mller, R.D.: The evolution of basal mantle structure in response to supercontinent aggregation and dispersal. Scientific Reports **11**(1), 22967 (2021) https://doi.org/10.1038/s41598-021-02359-z . Number: 1 Publisher: Nature Publishing Group. Accessed 2023-03-08

[7] Grabreck, A., Flament, N., Bodur, .F.: Mapping global kimberlite potential from reconstructions of mantle flow over the past billion years. PLOS ONE **17**(6), 0268066 (2022) https://doi.org/10.1371/journal.pone.0268066 . Publisher: Public Library of Science. Accessed 2023-03-07

[8] Cottaar, S., Lekic, V.: Morphology of seismically slow lower-mantle structures. Geophysical Journal International **207**(2), 1122–1136 (2016) https://doi.org/10.1093/gji/ggw324 . Accessed 2023-07-12

[9] Wang, Y., Wen, L.: Geometry and P and S velocity structure of the African Anomaly. Journal of Geophysical Research: Solid Earth **112**(B5) (2007) https://doi.org/10.1029/2006JB004483 . _eprint: https://onlinelibrary.wiley.com/doi/pdf/10.1029/2006JB004483. Accessed 2023-07-12

[10] He, Y., Wen, L.: Structural features and shear-velocity structure of the Pacific Anomaly. Journal of Geophysical Research: Solid Earth **114**(B2) (2009) https://doi.org/10.1029/2008JB005814 . _eprint: https://onlinelibrary.wiley.com/doi/pdf/10.1029/2008JB005814. Accessed 2023-07-12

[11] Jackson, M.G., Becker, T.W., Konter, J.G.: Geochemistry and Distribution of Recycled Domains in the Mantle Inferred From Nd and Pb Isotopes in Oceanic Hot Spots: Implications for Storage in the Large Low Shear Wave Velocity Provinces. Geochemistry, Geophysics, Geosystems **19**(9), 3496–3519 (2018) https://doi.org/10.1029/2018GC007552 . _eprint: https://onlinelibrary.wiley.com/doi/pdf/10.1029/2018GC007552. Accessed 2023-03-08

[12] Richards, F.D., Hoggard, M.J., Ghelichkhan, S., Koelemeijer, P., Lau, H.C.P.: Geodynamic, geodetic, and seismic constraints favour deflated and dense-cored LLVPs. Earth and Planetary Science Letters **602**, 117964 (2023) https://doi.org/10.1016/j.epsl.2022.117964 . Accessed 2023-03-02

[13] Zhang, Z., Dorfman, S.M., Labidi, J., Zhang, S., Li, M., Manga, M., Stixrude, L., McDonough, W.F., Williams, Q.: Primordial metallic melt in the deep mantle. Geophysical Research Letters **43**(8), 3693–3699 (2016) https://doi.org/10.1002/2016GL068560 . _eprint: https://onlinelibrary.wiley.com/doi/pdf/10.1002/2016GL068560

[14] Gleeson, M., Soderman, C., Matthews, S., Cottaar, S., Gibson, S.: Geochemical Constraints on the Structure of the Earth's Deep Mantle and the Origin of the LLSVPs. Geochemistry, Geophysics, Geosystems **22**(9), 2021–009932 (2021) https://doi.org/10.1029/2021GC009932 . _eprint: https://onlinelibrary.wiley.com/doi/pdf/10.1029/2021GC009932. Accessed 2023-03-07

[15] Tolstikhin, I., Hofmann, A.W.: Early crust on top of the Earth's core. Physics of the Earth and Planetary Interiors **148**(2), 109–130 (2005) https://doi.org/10.1016/j.pepi.2004.05.011 . Accessed 2023-06-06

[16] Lee, C.-T.A., Luffi, P., Hink, T., Li, J., Dasgupta, R., Hernlund, J.: Upside-down differentiation and generation of a primordial lower mantle. Nature **463**(7283), 930–933 (2010) https://doi.org/10.1038/nature08824 . Number: 7283 Publisher: Nature Publishing Group. Accessed 2023-06-06

[17] Yuan, Q., Li, M., Desch, S.J., Ko, B., Deng, H., Garnero, E.J., Gabriel, T.S.J., Kegerreis, J.A., Miyazaki, Y., Eke, V., Asimow, P.D.: Moon-forming impactor as a source of Earths basal mantle anomalies. Nature **623**(7985), 95–99 (2023) https://doi.org/10.1038/s41586-023-06589-1 . Number: 7985 Publisher: Nature Publishing Group

[18] Jones, T.D., Maguire, R.R., Van Keken, P.E., Ritsema, J., Koelemeijer, P.: Subducted oceanic crust as the origin of seismically slow lower-mantle structures. Progress in Earth and Planetary Science **7**, 17 (2020) https://doi.org/10.1186/s40645-020-00327-1

[19] Niu, Y., Wilson, M., Humphreys, E.R., OHara, M.J.: A trace element perspective on the source of ocean island basalts (OIB) and fate of subducted ocean crust (SOC) and mantle lithosphere (SML). Episodes Journal of International Geoscience **35**(2), 310–327 (2012) https://doi.org/10.18814/epiiugs/2012/v35i2/002 . Publisher: International Union of Geological Sciences

[20] Mulyukova, E., Steinberger, B., Dabrowski, M., Sobolev, S.V.: Survival of LLSVPs for billions of years in a vigorously convecting mantle: Replenishment and destruction of chemical anomaly. Journal of Geophysical Research: Solid Earth **120**(5), 3824–3847 (2015) https://doi.org/10.1002/2014JB011688 . Publisher: Blackwell Publishing Ltd

[21] Panton, J., Davies, J.H., Myhill, R.: The Stability of Dense Oceanic Crust Near the Core-Mantle Boundary. Journal of Geophysical Research: Solid Earth **128**(2), 2022–025610 (2023) https://doi.org/10.1029/2022JB025610 . _eprint: https://onlinelibrary.wiley.com/doi/pdf/10.1029/2022JB025610. Accessed 2023-03-09

[22] Li, Y., Deschamps, F., Tackley, P.J.: The stability and structure of primordial reservoirs in the lower mantle: insights from models of thermochemical convection in three-dimensional spherical geometry. Geophys. J. Int. **199**(2), 914–930 (2014) https://doi.org/10.1093/gji/ggu295

[23] Cao, X., Flament, N., Mller, R.D.: Coupled Evolution of Plate Tectonics and Basal Mantle Structure. Geochemistry, Geophysics, Geosystems **22**(1), 2020–009244 (2021) https://doi.org/10.1029/2020GC009244 . _eprint: https://onlinelibrary.wiley.com/doi/pdf/10.1029/2020GC009244. Accessed 2023-03-08

[24] Guerrero, J.M., Deschamps, F., Li, Y., Hsieh, W.-P., Tackley, P.J.: Influence of heterogeneous thermal conductivity on the long-term evolution of the lower-mantle thermochemical structure: implications for primordial reservoirs. Solid Earth **14**(2), 119–135 (2023) https://doi.org/10.5194/se-14-119-2023 . Publisher: Copernicus GmbH. Accessed 2024-09-11

[25] Christensen, U.R., Hofmann, A.W.: Segregation of subducted oceanic crust in the convecting mantle. Journal of Geophysical Research: Solid Earth **99**(B10), 19867–19884 (1994) https://doi.org/10.1029/93JB03403 . ISBN: 2156-2202

[26] Huang, C., Leng, W., Wu, Z.: The continually stable subduction, iron-spin transition, and the formation of llsvps from subducted oceanic crust. Journal of Geophysical Research: Solid Earth **125**(1),

2019–018262 (2020) https://doi.org/10.1029/2019JB018262 . _eprint: https://onlinelibrary.wiley.com/doi/pdf/10.1029/2019JB018262

[27] Li, M., McNamara, A.K.: The difficulty for subducted oceanic crust to accumulate at the earth's core-mantle boundary. Journal of Geophysical Research: Solid Earth **118**(4), 1807–1816 (2013) https://doi.org/10.1002/jgrb.50156

[28] Baumgardner, J.R.: Three-dimensional treatment of convective flow in the earth's mantle. Journal of Statistical Physics **39**(5-6), 501–511 (1985) https://doi.org/10.1007/BF01008348

[29] Bunge, H.-P., Baumgardner, J.R.: Mantle convection modeling on parallel virtual machines. Computers in Physics **9**(2), 207 (1995) https://doi.org/10.1063/1.168525

[30] Mller, R.D., Flament, N., Cannon, J., Tetley, M.G., Williams, S.E., Cao, X., Bodur, .F., Zahirovic, S., Merdith, A.: A tectonic-rules-based mantle reference frame since 1 billion years ago implications for supercontinent cycles and plate-mantle system evolution. Solid Earth **13**(7), 1127–1159 (2022) https://doi.org/10.5194/se-13-1127-2022 . Publisher: Copernicus GmbH. Accessed 2023-02-13

[31] Merdith, A.S., Williams, S.E., Collins, A.S., Tetley, M.G., Mulder, J.A., Blades, M.L., Young, A., Armistead, S.E., Cannon, J., Zahirovic, S., Mller, R.D.: Extending full-plate tectonic models into deep time: Linking the Neoproterozoic and the Phanerozoic. Earth-Science Reviews **214**, 103477 (2021) https://doi.org/10.1016/j.earscirev.2020.103477 . Publisher: Elsevier B.V.

[32] Heck, H.J., Davies, J.H., Elliott, T., Porcelli, D.: Global-scale modelling of melting and isotopic evolution of Earth's mantle: Melting modules for TERRA. Geoscientific Model Development **9**(4), 1399–1411 (2016) https://doi.org/10.5194/gmd-9-1399-2016

[33] Price, M.G., Davies, J.H., Panton, J.: Controls on the Deep-Water Cycle Within Three-Dimensional Mantle Convection Models. Geochemistry, Geophysics, Geosystems **20**(5) (2019) https://doi.org/10.1029/2018GC008158

[34] Panton, J., Davies, J.H., Elliott, T., Andersen, M., Porcelli, D., Price, M.G.: Investigating Influences on the Pb Pseudo-Isochron Using Three-Dimensional Mantle Convection Models With a Continental Reservoir. Geochemistry, Geophysics, Geosystems **23**(8), 2021–010309 (2022) https://doi.org/10.1029/2021GC010309 . _eprint: https://onlinelibrary.wiley.com/doi/pdf/10.1029/2021GC010309. Accessed 2023-03-09

[35] Ritsema, J., Deuss, A., Van Heijst, H.J., Woodhouse, J.H.: S40RTS: A degree-40 shear-velocity model for the mantle from new Rayleigh wave dispersion, teleseismic traveltime and normal-mode splitting function measurements. Geophysical Journal International **184**(3), 1223–1236 (2011) https://doi.org/10.

1111/J.1365-246X.2010.04884.X

[36] Wang, W., Xu, Y., Sun, D., Ni, S., Wentzcovitch, R., Wu, Z.: Velocity and density characteristics of subducted oceanic crust and the origin of lower-mantle heterogeneities. Nature Communications 2020 11:1 **11**(1), 1–8 (2020) https://doi.org/10.1038/s41467-019-13720-2 . Publisher: Nature Publishing Group

[37] Tsuchiya, T.: Elasticity of subducted basaltic crust at the lower mantle pressures: Insights on the nature of deep mantle heterogeneity. Physics of the Earth and Planetary Interiors **188**(3-4), 142–149 (2011) https://doi.org/10.1016/J.PEPI.2011.06.018 . Publisher: Elsevier

[38] Ricolleau, A., Perrillat, J.-P., Fiquet, G., Daniel, I., Matas, J., Addad, A., Menguy, N., Cardon, H., Mezouar, M., Guignot, N.: Phase relations and equation of state of a natural MORB: Implications for the density profile of subducted oceanic crust in the Earth's lower mantle. Journal of Geophysical Research: Solid Earth **115**(B8), 8202 (2010) https://doi.org/10.1029/2009JB006709 . Publisher: John Wiley & Sons, Ltd

[39] Rudolph, M.L., Loureno, D.L., Moulik, P., Leki, V.: Long-Wavelength Mantle Structure. In: Mantle Convection and Surface Expressions, pp. 1–19. American Geophysical Union (AGU), ??? (2021). https://doi.org/10.1002/9781119528609.ch1 . https://onlinelibrary.wiley.com/doi/abs/10.1002/9781119528609.ch1 Accessed 2024-07-24

[40] Nomura, R., Hirose, K., Uesugi, K., Ohishi, Y., Tsuchiyama, A., Miyake, A., Ueno, Y.: Low Core-Mantle Boundary Temperature Inferred from the Solidus of Pyrolite. Science **343**(6170), 522–525 (2014) https://doi.org/10.1126/science.1248186 . Accessed 2024-07-24

[41] Alf, D., Gillan, M.J., Price, G.D.: Temperature and composition of the Earth's core. Contemporary Physics **48**(2), 63–80 (2007) https://doi.org/10.1080/00107510701529653 . Accessed 2024-07-24

[42] Becker, T.W., Boschi, L.: A comparison of tomographic and geodynamic mantle models. Geochemistry, Geophysics, Geosystems **3**(1) (2002) https://doi.org/10.1029/2001GC000168 . _eprint: https://onlinelibrary.wiley.com/doi/pdf/10.1029/2001GC000168. Accessed 2023-03-16

[43] Shephard, G.E., Matthews, K.J., Hosseini, K., Domeier, M.: On the consistency of seismically imaged lower mantle slabs. Scientific Reports **7**(1), 10976 (2017) https://doi.org/10.1038/s41598-017-11039-w . Publisher: Nature Publishing Group. Accessed 2024-07-25

[44] Hosseini, K., Matthews, K.J., Sigloch, K., Shephard, G.E., Domeier, M., Tsekhmistrenko, M.: SubMachine: Web-Based Tools

for Exploring Seismic Tomography and Other Models of Earth's Deep Interior. Geochemistry, Geophysics, Geosystems **19**(5), 1464–1483 (2018) https://doi.org/10.1029/2018GC007431 . _eprint: https://onlinelibrary.wiley.com/doi/pdf/10.1029/2018GC007431. Accessed 2023-07-07

[45] Yuan, Q., Li, M.: Instability of the African large low-shear-wave-velocity province due to its low intrinsic density. Nature Geoscience **15**(4), 334–339 (2022) https://doi.org/10.1038/s41561-022-00908-3 . Number: 4 Publisher: Nature Publishing Group. Accessed 2023-02-09

[46] Li, Y., Deschamps, F., Tackley, P.J.: Effects of the post-perovskite phase transition properties on the stability and structure of primordial reservoirs in the lower mantle of the Earth. Earth and Planetary Science Letters **432**, 1–12 (2015) https://doi.org/10.1016/j.epsl.2015.09.040

[47] Doucet, L.S., Li, Z.-X., Gamal El Dien, H., Pourteau, A., Murphy, J.B., Collins, W.J., Mattielli, N., Olierook, H.K.H., Spencer, C.J., Mitchell, R.N.: Distinct formation history for deep-mantle domains reflected in geochemical differences. Nature Geoscience **13**(7), 511–515 (2020) https://doi.org/10.1038/s41561-020-0599-9 . Number: 7 Publisher: Nature Publishing Group. Accessed 2023-03-07

[48] Hassan, R., Flament, N., Gurnis, M., Bower, D.J., Mller, D.: Provenance of plumes in global convection models. Geochemistry, Geophysics, Geosystems **16**(5), 1465–1489 (2015) https://doi.org/10.1002/2015GC005751 . Publisher: John Wiley & Sons, Ltd. Accessed 2022-08-04

[49] Jackson, M.G., Becker, T.W., Steinberger, B.: Spatial Characteristics of Recycled and Primordial Reservoirs in the Deep Mantle. Geochemistry, Geophysics, Geosystems **22**(3), 2020–009525 (2021) https://doi.org/10.1029/2020GC009525 . _eprint: https://onlinelibrary.wiley.com/doi/pdf/10.1029/2020GC009525. Accessed 2023-03-08

[50] Ritsema, J., McNamara, A.K., Bull, A.L.: Tomographic filtering of geodynamic models: Implications for models interpretation and large-scale mantle structure. Journal of Geophysical Research: Solid Earth **112**(1) (2007) https://doi.org/10.1029/2006JB004566

[51] Ritsema, J., Van Heijst, H.J., Woodhouse, J.H., Deuss, A.: Long-period body wave traveltimes through the crust: implication for crustal corrections and seismic tomography. Geophysical Journal International **179**(2), 1255–1261 (2009) https://doi.org/10.1111/j.1365-246X.2009.04365.x . Accessed 2024-04-26

[52] Karato, S.-i., Karki, B.B.: Origin of lateral variation of seismic wave velocities and density in the deep mantle. Journal of Geophysical Research: Solid Earth **106**(B10), 21771–21783 (2001) https://doi.org/10.1029/2001JB000214 .

Publisher: John Wiley & Sons, Ltd

[53] Koelemeijer, P., Deuss, A., Ritsema, J.: Density structure of Earths lowermost mantle from Stoneley mode splitting observations. Nature Communications **8**(1), 15241 (2017) https://doi.org/10.1038/ncomms15241 . Publisher: Nature Publishing Group. Accessed 2024-03-15

[54] Jones, T.D., Sime, N., Keken, P.E.: Burying Earth's Primitive Mantle in the Slab Graveyard. Geochemistry, Geophysics, Geosystems **22**(3), 2020–009396 (2021) https://doi.org/10.1029/2020GC009396 . _eprint: https://onlinelibrary.wiley.com/doi/pdf/10.1029/2020GC009396. Accessed 2023-03-07

[55] Glcher, A.J.P., Ballmer, M.D., Tackley, P.J.: Coupled dynamics and evolution of primordial and recycled heterogeneity in Earth's lower mantle. Solid Earth **12**(9), 2087–2107 (2021) https://doi.org/10.5194/se-12-2087-2021

[56] Stixrude, L., Lithgow-Bertelloni, C.: Thermal expansivity, heat capacity and bulk modulus of the mantle. Geophysical Journal International **228**(2), 1119–1149 (2022) https://doi.org/10.1093/gji/ggab394 . Accessed 2023-03-07

[57] Badro, J., Fiquet, G., Guyot, F., Rueff, J.-P., Struzhkin, V.V., Vank, G., Monaco, G.: Iron partitioning in earth's mantle: Toward a deep lower mantle discontinuity. Science **300**(5620), 789–791 (2003) https://doi.org/10.1126/science.1081311 . Publisher: American Association for the Advancement of Science. Accessed 2024-03-15

[58] Ammann, M.W., Brodholt, J.P., Dobson, D.P.: Ferrous iron diffusion in ferropericlase across the spin transition. Earth and Planetary Science Letters **302**(3), 393–402 (2011) https://doi.org/10.1016/j.epsl.2010.12.031 . Accessed 2024-03-15

[59] Trautner, V.E., Stackhouse, S., Turner, A.R., Koelemeijer, P., Davies, D.R., Mndez, A.S.J., Satta, N., Kurnosov, A., Liermann, H.-P., Marquardt, H.: Compressibility of ferropericlase at high-temperature: Evidence for the iron spin crossover in seismic tomography. Earth and Planetary Science Letters **618**, 118296 (2023) https://doi.org/10.1016/j.epsl.2023.118296 . Accessed 2024-04-26

[60] Stixrude, L., Lithgow-Bertelloni, C.: Thermodynamics of mantle minerals - II. Phase equilibria. Geophysical Journal International **184**(3), 1180–1213 (2011) https://doi.org/10.1111/j.1365-246X.2010.04890.x https://academic.oup.com/gji/article-pdf/184/3/1180/27638878/184-3-1180.pdf

[61] Bunge, H.-P., Richards, M.A., Baumgardner, J.R.: A sensitivity study of three-dimensional spherical mantle convection at 10 8 Rayleigh number: Effects of depth-dependent viscosity, heating mode, and an endothermic phase change. Journal of Geophysical Research: Solid Earth **102**(B6), 11991–12007 (1997)

https://doi.org/10.1029/96JB03806 . ISBN: 0148-0227

[62] Bunge, H.-P., Hagelberg, C.R., Travis, B.J.: Mantle circulation models with variational data assimilation: inferring past mantle flow and structure from plate motion histories and seismic tomography. Geophysical Journal International **152**(2), 280–301 (2003) https://doi.org/10.1046/j.1365-246X.2003.01823.x . Accessed 2020-11-30

[63] McKenzie, D.P., Roberts, J.M., Weiss, N.O.: Convection in the earth's mantle: Towards a numerical simulation. Journal of Fluid Mechanics **62**(3), 465–538 (1974) https://doi.org/10.1017/S0022112074000784 . ISBN: 0022-1120

[64] Li, M., McNamara, A.K.: The difficulty for subducted oceanic crust to accumulate at the Earth's core-mantle boundary. Journal of Geophysical Research: Solid Earth **118**(4), 1807–1816 (2013) https://doi.org/10.1002/jgrb.50156 . Accessed 2024-07-16

[65] Bunge, H.-P., Richards, M.A., Baumgardner, J.R.: Mantlecirculation models with sequential data assimilation: inferring presentday mantle structure from platemotion histories. Philosophical Transactions of the Royal Society of London. Series A: Mathematical, Physical and Engineering Sciences **360**(1800), 2545–2567 (2002) https://doi.org/10.1098/rsta.2002.1080 . Publisher: Royal Society

[66] Keken, P.E., Ballentine, C.J.: Whole-mantle versus layered mantle convection and the role of a high-viscosity lower mantle in terrestrial volatile evolution. Earth and Planetary Science Letters **156**(1-2), 19–32 (1998) https://doi.org/10.1016/s0012-821x(98)00023-5

[67] Baker, M.B., Beckett, J.R.: The origin of abyssal peridotites: a reinterpretation of constraints based on primary bulk compositions. Earth and Planetary Science Letters **171**(1), 49–61 (1999) https://doi.org/10.1016/S0012-821X(99)00130-2

[68] Walter, M.J.: 2.08 - Melt Extraction and Compositional Variability in Mantle Lithosphere. In: Holland, H.D., Turekian, K.K. (eds.) Treatise on Geochemistry, pp. 363–394. Pergamon, Oxford (2003). https://doi.org/10.1016/B0-08-043751-6/02008-9 . https://www.sciencedirect.com/science/article/pii/B0080437516020089 Accessed 2024-03-18

[69] White, W.M., Klein, E.M.: 4.13 - Composition of the Oceanic Crust. In: Holland, H.D., Turekian, K.K. (eds.) Treatise on Geochemistry (Second Edition), pp. 457–496. Elsevier, Oxford (2014). https://doi.org/10.1016/B978-0-08-095975-7.00315-6

[70] Wolstencroft, M., Huw Davies, J.: Breaking supercontinents; No need to choose between passive or active. Solid Earth **8**(4), 817–825 (2017) https://doi.org/10.5194/se-8-817-2017

[71] Hirose, K., Takafuji, N., Sata, N., Ohishi, Y.: Phase transition and density of subducted MORB crust in the lower mantle. Earth and Planetary Science Letters **237**(1-2), 239–251 (2005) https://doi.org/10.1016/j.epsl.2005.06.035

[72] Connolly, J.a.D.: The geodynamic equation of state: What and how. Geochemistry, Geophysics, Geosystems **10**(10) (2009) https://doi.org/10.1029/2009GC002540 . _eprint: https://onlinelibrary.wiley.com/doi/pdf/10.1029/2009GC002540. Accessed 2023-04-21

[73] Goes, S., Cammarano, F., Hansen, U.: Synthetic seismic signature of thermal mantle plumes. Earth and Planetary Science Letters **218**(3), 403–419 (2004) https://doi.org/10.1016/S0012-821X(03)00680-0 . Accessed 2023-07-20

[74] Maguire, R., Ritsema, J., Keken, P.E., Fichtner, A., Goes, S.: P- and S-wave delays caused by thermal plumes. Geophysical Journal International **206**(2), 1169–1178 (2016) https://doi.org/10.1093/gji/ggw187 . Accessed 2023-07-20

[75] Xu, W., Lithgow-Bertelloni, C., Stixrude, L., Ritsema, J.: The effect of bulk composition and temperature on mantle seismic structure. Earth and Planetary Science Letters **275**(1-2), 70–79 (2008) https://doi.org/10.1016/j.epsl.2008.08.012 . ISBN: 0012-821X

[76] Davies, D.R., Goes, S., Davies, J.H., Schuberth, B.S.A., Bunge, H.P., Ritsema, J.: Reconciling dynamic and seismic models of Earth's lower mantle: The dominant role of thermal heterogeneity. Earth and Planetary Science Letters **353-354**, 253–269 (2012) https://doi.org/10.1016/j.epsl.2012.08.016 . Publisher: Elsevier ISBN: 0012-821X

[77] Davies, D.R.: Thermally dominated deep mantle LLSVPs: A review (2015) https://doi.org/10.1007/978-3-319-15627-9_14

[78] Peng, D., Liu, L.: Quantifying slab sinking rates using global geodynamic models with data-assimilation. Earth-Science Reviews **230**, 104039 (2022) https://doi.org/10.1016/j.earscirev.2022.104039

[79] Pedregosa, F., Varoquaux, G., Gramfort, A., Michel, V., Thirion, B., Grisel, O., Blondel, M., Prettenhofer, P., Weiss, R., Dubourg, V., Vanderplas, J., Passos, A., Cournapeau, D., Brucher, M., Perrot, M., Duchesnay, .: Scikit-learn: Machine Learning in Python. Journal of Machine Learning Research **12**(85), 2825–2830 (2011). Accessed 2023-07-28

[80] Crameri, F., Shephard, G.E., Heron, P.J.: The misuse of colour in science communication. Nature Communications **11**(1), 1–10 (2020) https://doi.org/10.1038/s41467-020-19160-7 . Publisher: Nature Research. Accessed 2021-01-29

Supplementary Information for: Unique composition and evolutionary histories of large low velocity provinces

James Panton[1*], J. Huw Davies[1], Paula Koelemeijer[2], Robert Myhill[3], Jeroen Ritsema[4]

[1*]School of Earth and Environmental Sciences, Cardiff University, Park Place, Cardiff, CF10 3AT, Wales, UK.
[2]Department of Earth Sciences, University of Oxford, South Parks Road, Oxford, OX1 3AN, England, UK.
[3]School of Earth Sciences, University of Bristol, Queens Road, Bristol, BS8 1RJ, England, UK.
[4]Department of Earth and Environmental Sciences, University of Michigan, 1100 North University Avenue, Ann Arbor, 40819, MI, USA.

*Corresponding author(s). E-mail(s): pantonjc@cardiff.ac.uk;

Content

Supplementary Figures

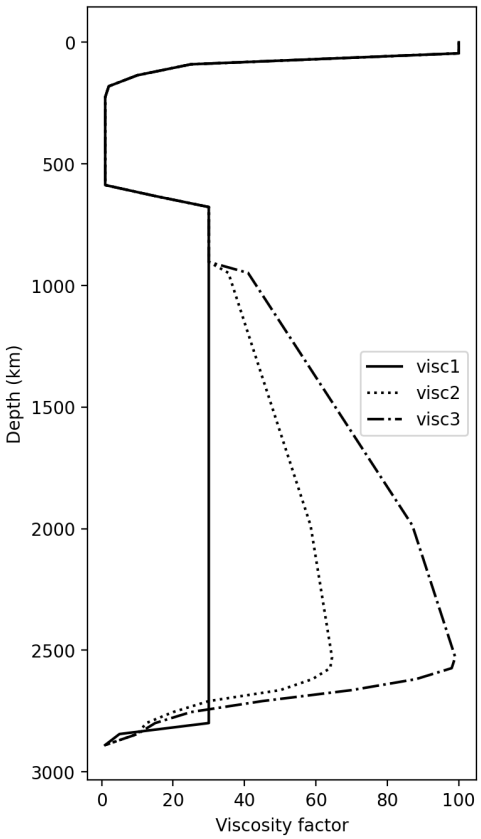

Fig. S1 Radial profile of the viscosity scaling factors used in the simulations listed in Table 1 of the main text.

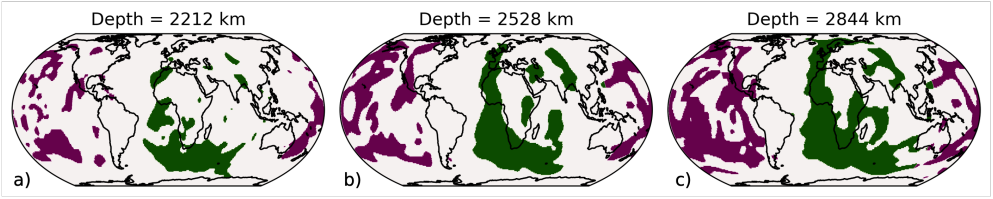

Fig. S2 Depth slices at 2212 km (a), 2528 km (b) and 2844 (km) to illustrate the identification of areas as S-LLVPs in the Pacific (purple) and African (green) regions for simulation RCY.

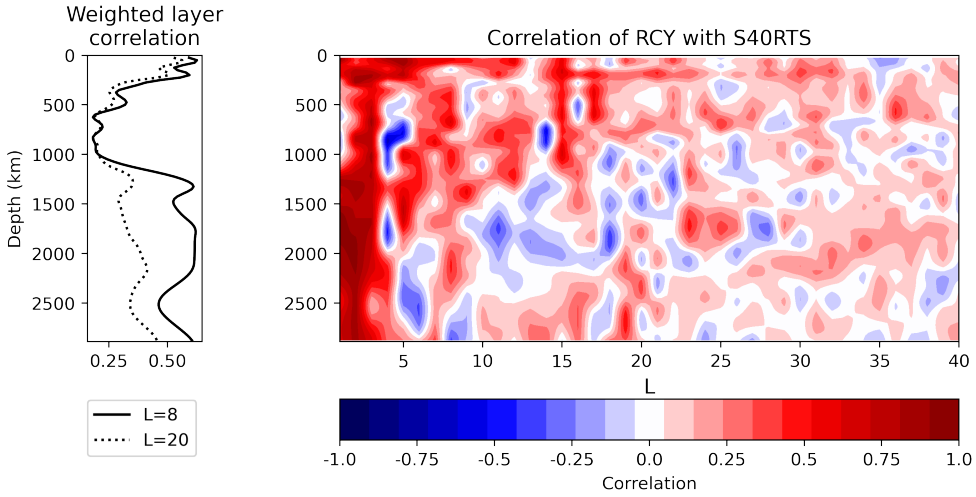

Fig. S3 Correlation between mantle structure predicted by simulation RCY and imaged by S40RTS versus depth and spherical harmonic degree, L (Methods 6.4), plotted up to $L = 40$ (right panel) or as a total weighted layer correlation up to $L = 8$ and $L = 20$ (left panel).

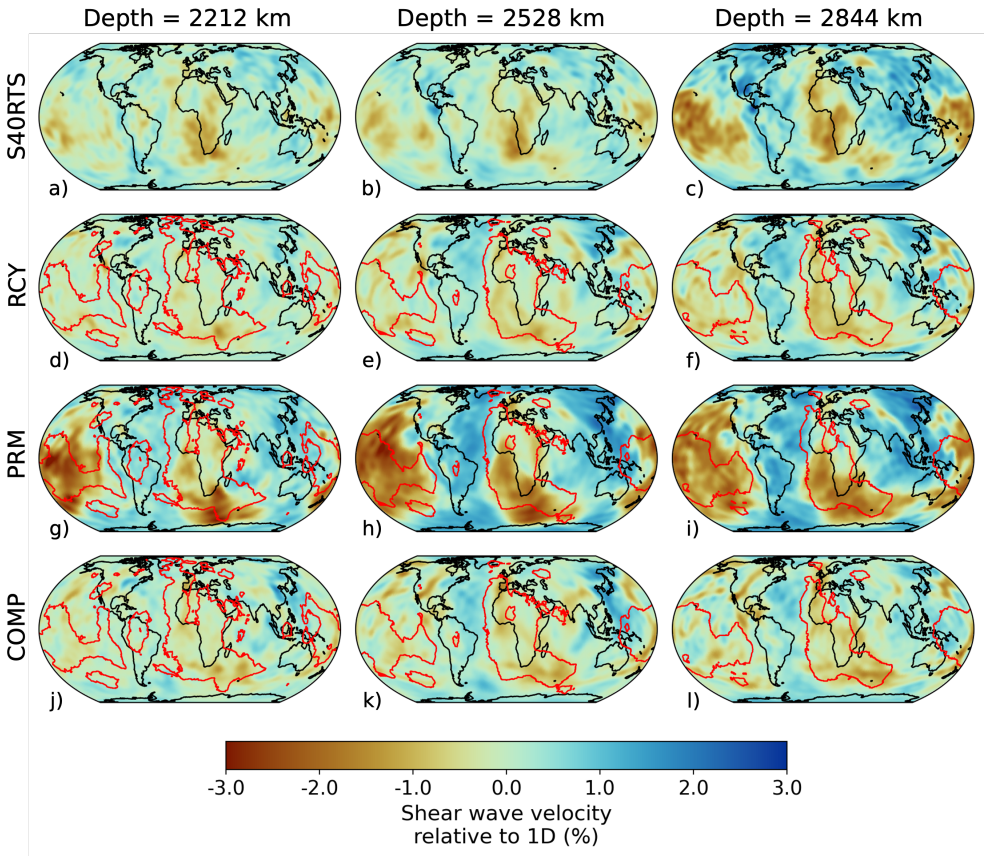

Fig. S4 Mantle structure at 2212 km (left column), 2528 km (centre column), and 2844 km (right column) depth, showing δV_s according to seismic tomography model S40RTS (a-c, top row), δV_s predicted in simulation RCY (d-f), δV_s predicted in simulation PRM (g-i) and δV_s predicted in simulation COMP (j-l), all filtered by the S40RTS resolution. Red outlines are derived from a vote map of low velocity regions detected in 18 shear wave tomography models [1, 2], indicating whereat least 5 models are in agreement.

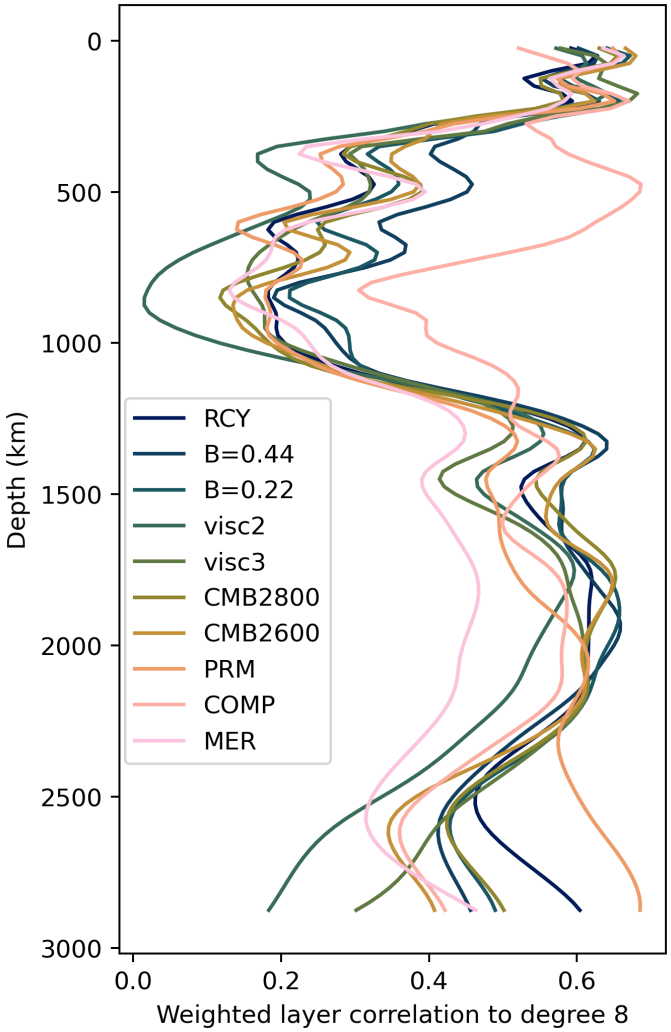

Fig. S5 Total weighted layer correlation (Methods 6.4) up to spherical harmonic degree $L = 8$ for all simulations.

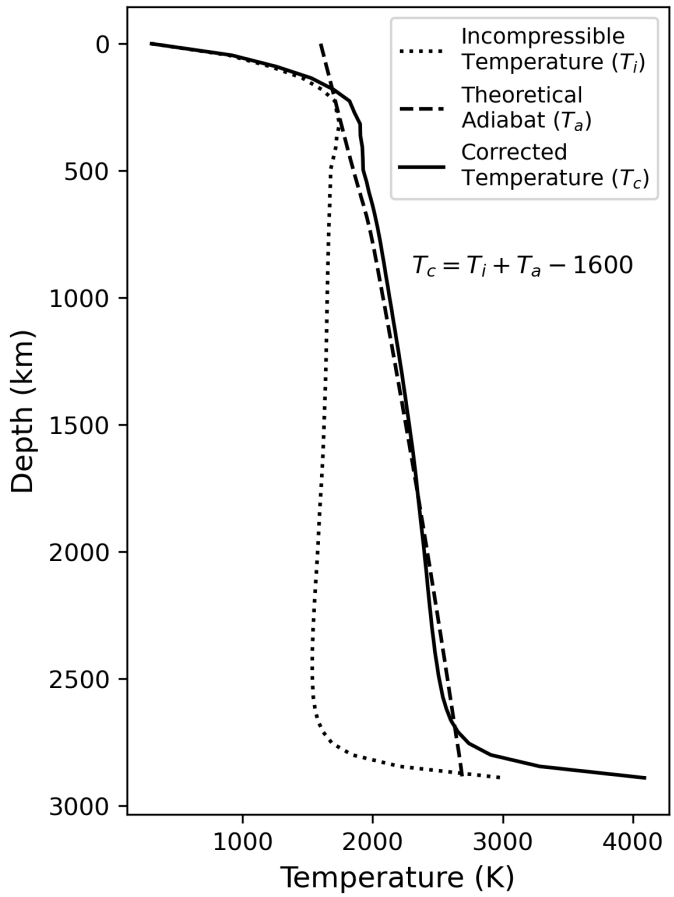

Fig. S6 Conversion of incompressible mantle temperature T_i to corrected temperature T_c using a theoretical adiabat.

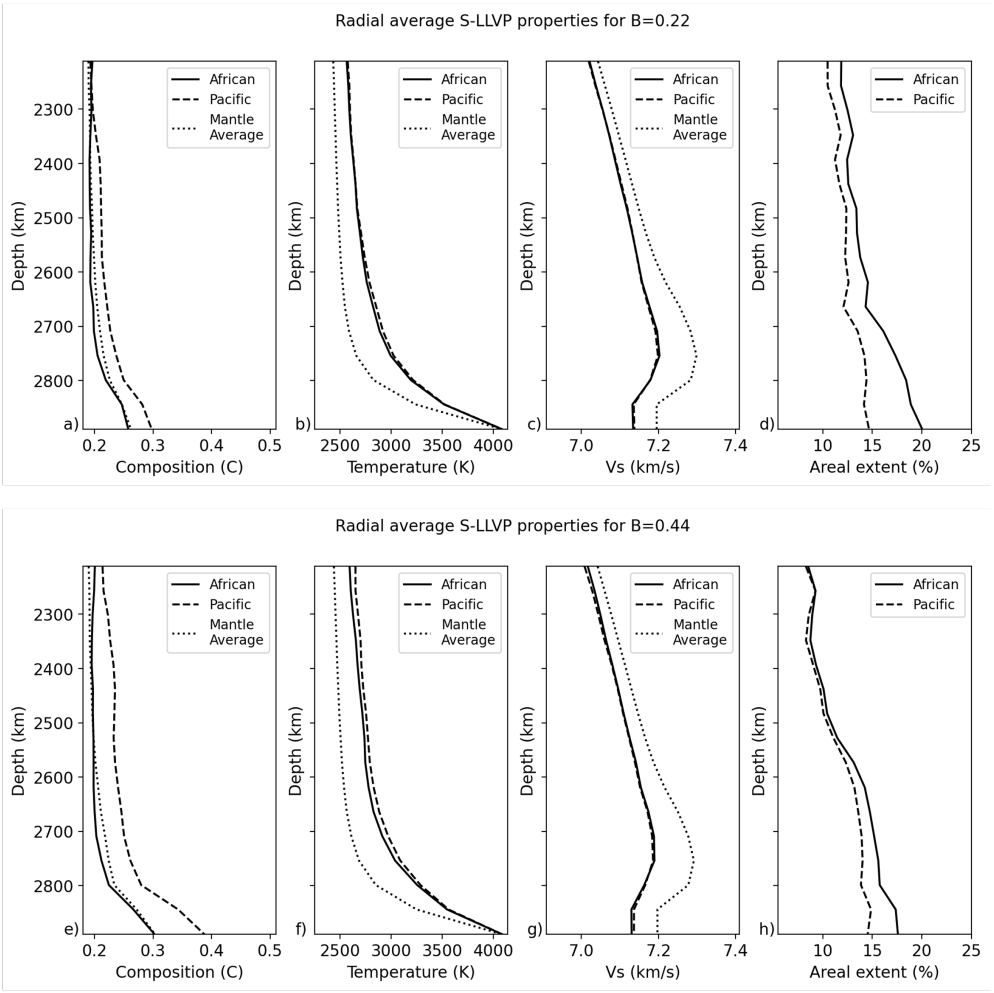

Fig. S7 Radial average of present day s-LLVP properties in simulations with different buoyancy numbers: (a-d) $B = 0.22$ and (e-h) $B = 0.44$, showing (a,e) bulk composition, (b,f) temperature, (c,g) predicted absolute shear-wave velocity (unfiltered), and (d,h) areal extent in each radial layer, for both the African (solid line) and Pacific (dashed line) S-LLVPs identified in the simulations. Similar to Fig. 2 in the main text.

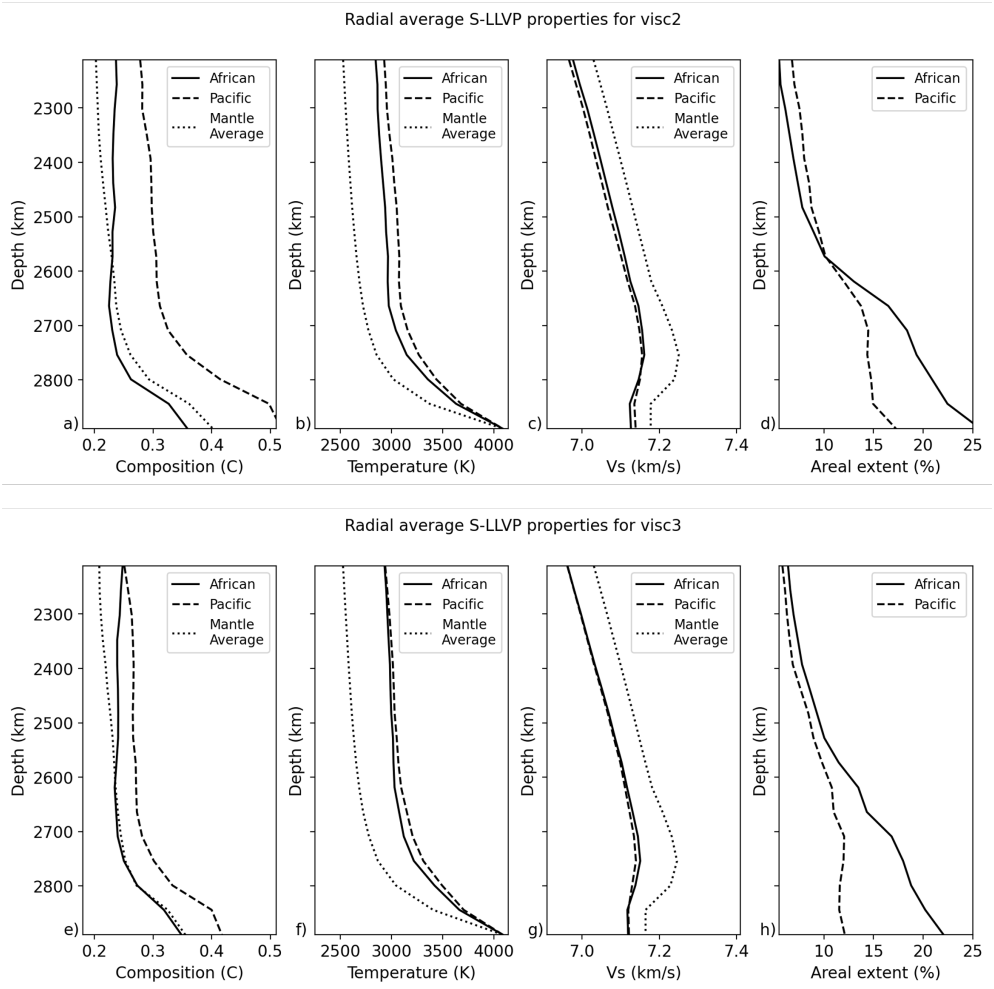

Fig. S8 Radial average of present day s-LLVP properties in simulations with different viscosity profiles: (a-d) visc2 and (e-h) visc3, showing (a,e) bulk composition, (b,f) temperature, (c,g) predicted absolute shear-wave velocity (unfiltered), and (d,h) areal extent in each radial layer, for both the African (solid line) and Pacific (dashed line) S-LLVPs identified in the simulations. Similar to Fig. S7 and Fig. 2 in the main text.

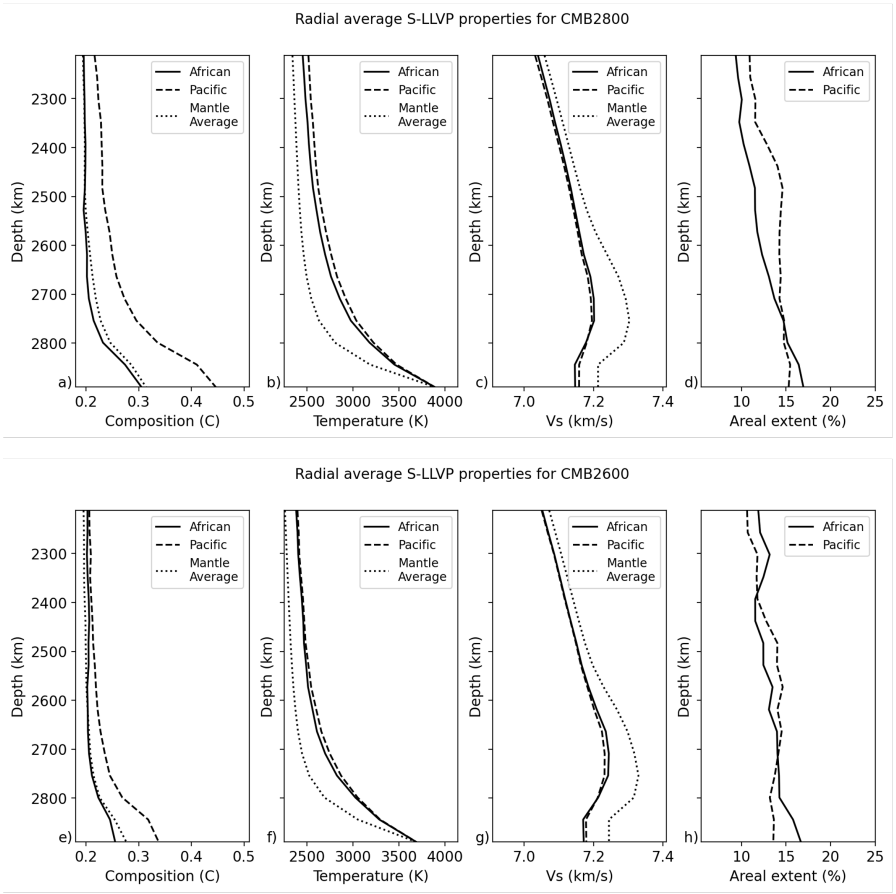

Fig. S9 Radial average of present day s-LLVP properties in simulations with different CMB temperatures: (a-d) CMB2800 and (e-h) CMB2600, showing (a,e) bulk composition, (b,f) temperature, (c,g) predicted absolute shear-wave velocity (unfiltered), and (d,h) areal extent in each radial layer, for both the African (solid line) and Pacific (dashed line) S-LLVPs identified in the simulations. Similar to Fig. S7-S8 and Fig. 2 in the main text.

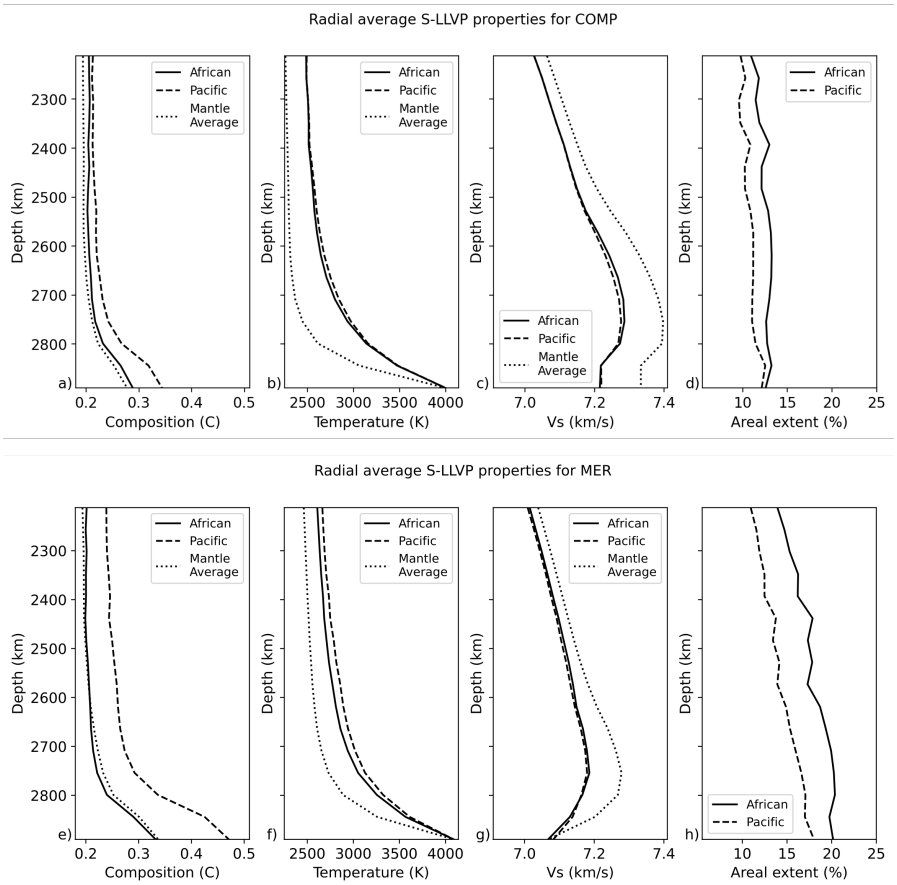

Fig. S10 Radial average of present day s-LLVP properties in simulations (a-d) COMP and (e-h) MER, showing (a,e) bulk composition, (b,f) temperature, (c,g) predicted absolute shear-wave velocity (unfiltered), and (d,h) areal extent in each radial layer, for both the African (solid line) and Pacific (dashed line) S-LLVPs identified in the simulations. Similar to Fig. S7-S9 and Fig. 2 in the main text.

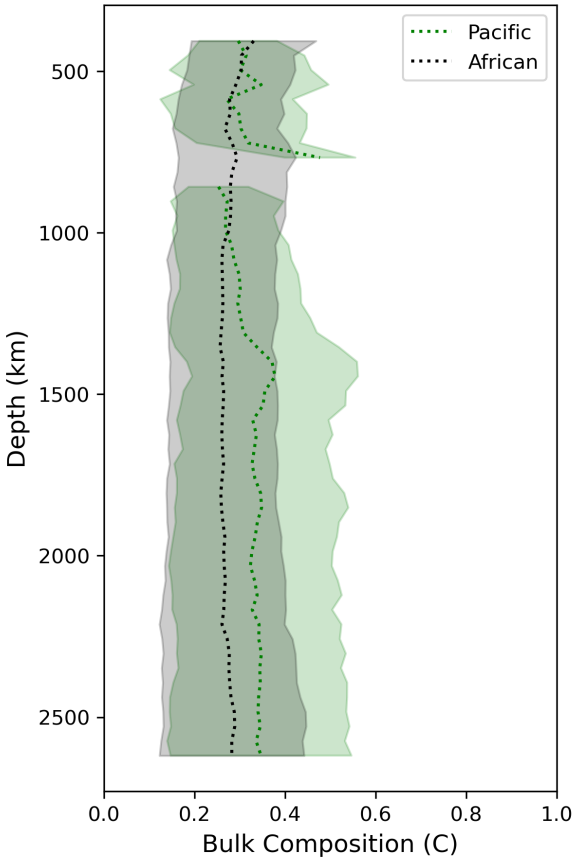

Fig. S11 Mean bulk composition of plumes associated with the Pacific and African s-LLVPs (dashed lines) in simulation RCY with ±1 standard deviation indicated by the shaded area.

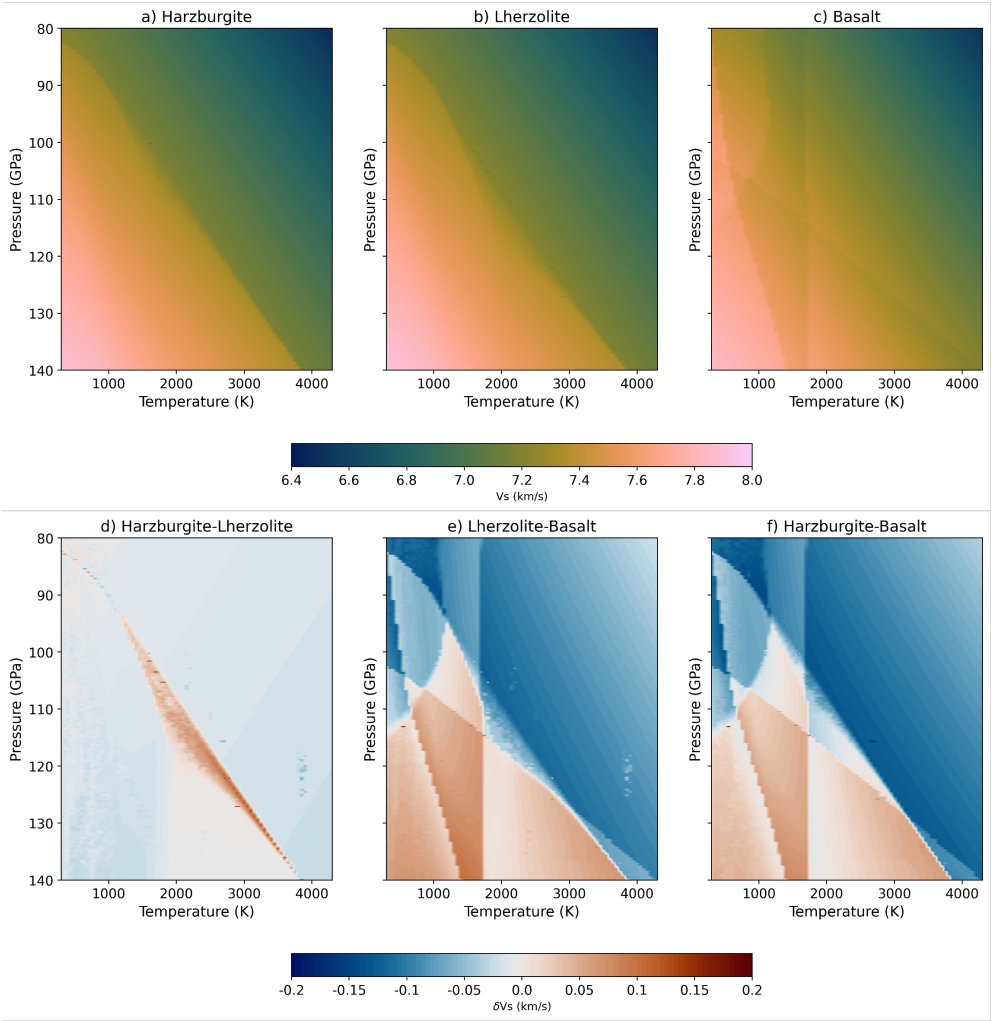

Fig. S12 Mineral physics estimates of the shear-wave velocity as a function of temperature and pressure. The top row show shows absolute V_s for the characteristic lithologies: (a) harzburgite, (b) lherzolite, and (c) basalt. The bottom row shows the differences in absolute V_s between (d) harzburgite and lherzolite, (e) lherzolite and basalt, and (f) harzburgite and basalt. See Methods 6.3 for full details of how the tables are produced.

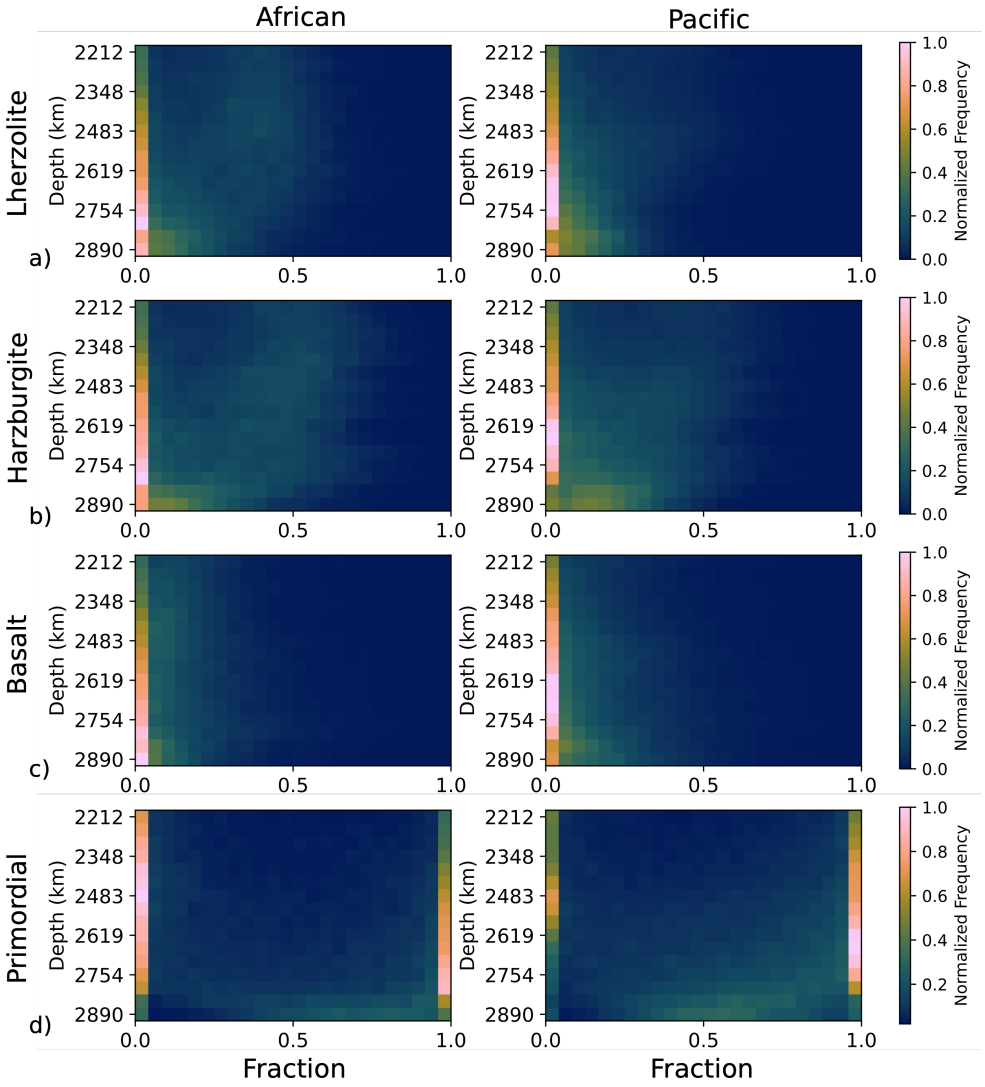

Fig. S13 Histograms for the proportions of different characteristic lithologies in the African (left column) and Pacific (right column) s-LLVPs in simulation PRM for each radial layer between 2212 km and 2890 km depth. The four characteristic lithologies are (a) harzburgite, (b) lherzolite, (c) basalt, and (d) the primordial component.

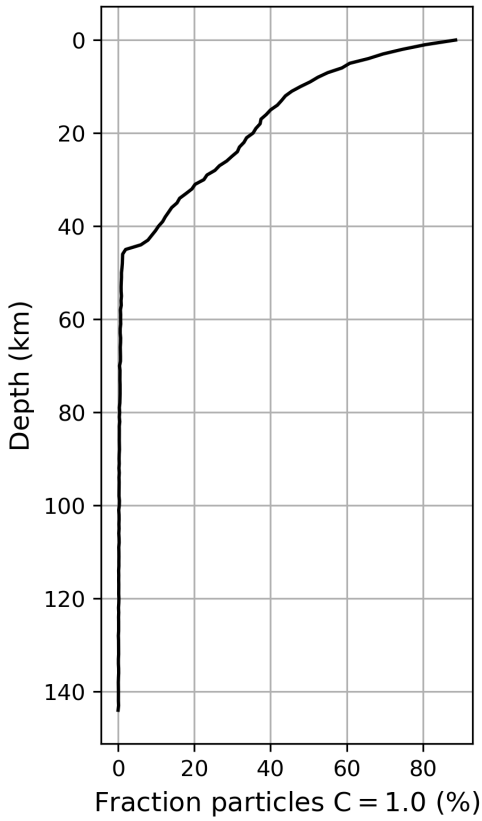

Fig. S14 Radial profile across the top 145 km of simulation RCY showing the fraction of particles within ocean basins that have a bulk composition of $C = 1.0$. The bottom of the oceanic crust is taken to be the depth at which 50% of particles in the ocean basins have a bulk composition of $C = 1$.

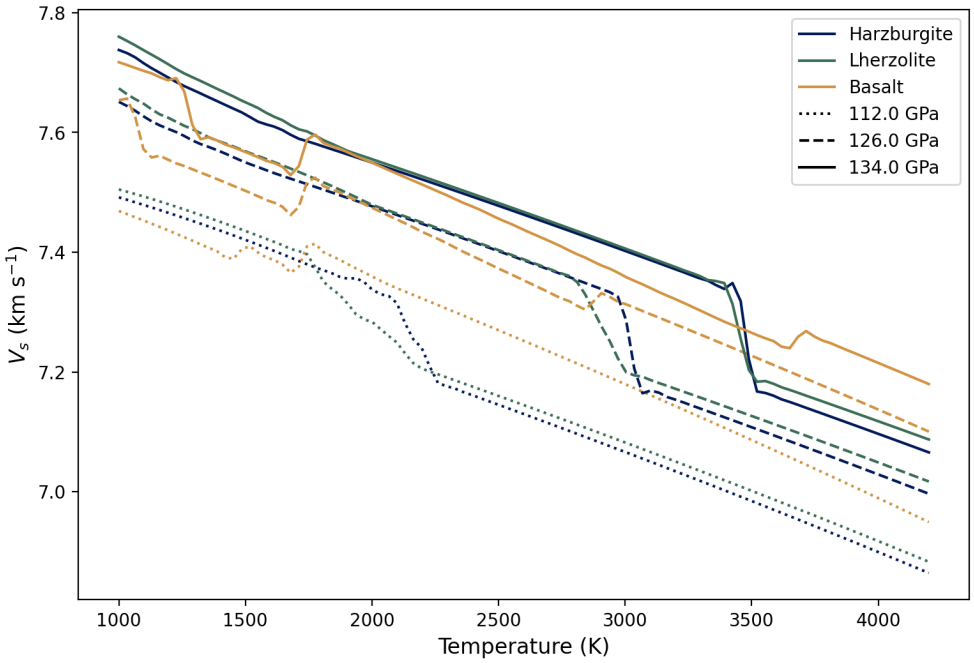

Fig. S15 Variation of predicted absolute V_s as a function of temperature at constant pressure, plotted for several characteristic lithologies: harzburgite (blue), lherzolite (green) and basalt (gold). Different lines indicate shear-wave velocities at different pressures: 134 GPa (solid line), 126 GPa (dashed line) and 112 GPa (dotted line).

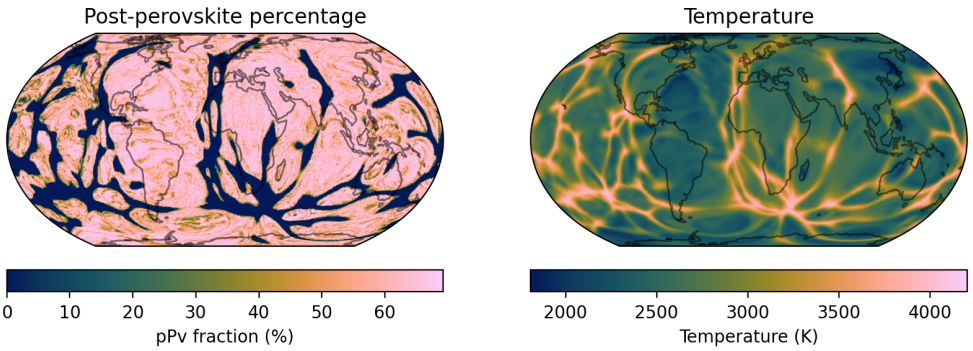

Fig. S16 Predicted distribution of post-perovskite in simulation RCY, shown at a depth of 2755 km. The left panel indicates the fraction of post-perovskite at this depth, the right panel shows the temperature field with an additional synthetic adiabat included.

Supplementary Video

Visualisation of case RCY.
Video SV1 https://youtu.be/hJLqbzRSpbY

References

[1] Shephard, G.E., Matthews, K.J., Hosseini, K., Domeier, M.: On the consistency of seismically imaged lower mantle slabs. Scientific Reports **7**(1), 10976 (2017) https://doi.org/10.1038/s41598-017-11039-w . Publisher: Nature Publishing Group. Accessed 2024-07-25

[2] Hosseini, K., Matthews, K.J., Sigloch, K., Shephard, G.E., Domeier, M., Tsekhmistrenko, M.: SubMachine: Web-Based Tools for Exploring Seismic Tomography and Other Models of Earth's Deep Interior. Geochemistry, Geophysics, Geosystems **19**(5), 1464–1483 (2018) https://doi.org/10.1029/2018GC007431 . _eprint: https://onlinelibrary.wiley.com/doi/pdf/10.1029/2018GC007431. Accessed 2023-07-07